

Journal of Materials Chemistry C

Accepted Manuscript



This is an *Accepted Manuscript*, which has been through the Royal Society of Chemistry peer review process and has been accepted for publication.

Accepted Manuscripts are published online shortly after acceptance, before technical editing, formatting and proof reading. Using this free service, authors can make their results available to the community, in citable form, before we publish the edited article. We will replace this *Accepted Manuscript* with the edited and formatted *Advance Article* as soon as it is available.

You can find more information about *Accepted Manuscripts* in the [Information for Authors](#).

Please note that technical editing may introduce minor changes to the text and/or graphics, which may alter content. The journal's standard [Terms & Conditions](#) and the [Ethical guidelines](#) still apply. In no event shall the Royal Society of Chemistry be held responsible for any errors or omissions in this *Accepted Manuscript* or any consequences arising from the use of any information it contains.

Critical roles of Mn-ions in enhancing insulation, piezoelectricity and multiferroicity of BiFeO₃-based lead-free high temperature ceramics

Yongquan Guo^a, Ping Xiao^a, Rui Wen^a, Yang Wan^a, Qiaoji Zheng^a, Dongliang Shi^b,
Kwok Ho Lam^b, Milan Liu^{*,c}, Dunmin Lin^{*,a}

^aCollege of Chemistry and Materials Science, Sichuan Normal University, Chengdu 610066, China

^bDepartment of Electrical Engineering, The Hong Kong Polytechnic University, Hunghom, Kowloon, Hong Kong

^cCollege of Physics, Jilin University, Changchun 130012, China

Abstract

Lead-free multiferroic ceramic of BiFe_{0.96}Sc_{0.04}O₃-BaTiO₃ is a member of ABO₃ perovskite structure, belonging to *R3c* space group, but exhibiting poor insulation and weak multiferroicity. In this work, the critical roles of Mn-ions in tailoring the electrical and magnetic properties of BiFeO₃-based materials are revealed: the introduction of MnO₂ into BiFe_{0.96}Sc_{0.04}O₃-BaTiO₃ induces a dramatic improvement in the insulation, piezoelectricity and multiferroicity. New compositions of BiFe_{0.96}Sc_{0.04}O₃-BaTiO₃ + *x* mol% MnO₂ were synthesized by a conventional

* Corresponding author: Tel.: +86 28 84760802; Fax: +86 28 84767868; liuml@jlu.edu.cn (Milan Liu), ddmd222@sicnu.edu.cn (Dunmin Lin)

solid-state reaction method. All the ceramics possess a perovskite structure, and a morphotropic phase boundary (MPB) of rhombohedral and monoclinic phases is formed at $x = 0.5-1.0$. The formation of $\text{Fe}_{\text{Fe}^{3+}}^{2+}$ and $\text{V}_{\text{O}^{2-}}^{\bullet\bullet}$ is noticeably suppressed and the resistivity of the ceramics is increased by ~ 100 times after the addition of 0.5-1.0 mol% MnO_2 , which make the ceramic polarizable and thus give strong ferroelectricity and considerable piezoelectricity. The ceramics located with MPB composition exhibit high electrical insulation ($R = 1.2-1.7 \times 10^{10} \Omega \cdot \text{cm}$), good piezoelectricity ($d_{33} = 123-143 \text{ pC/N}$, $k_p = 0.34-0.35$), strong ferroelectricity ($P_r = 13.1-17.6 \mu\text{C/cm}^2$), high Curie temperature ($590-596 \text{ }^\circ\text{C}$) and excellent temperature stability of piezoelectric and ferroelectric properties. These improvements are greatly associated with the contribution of Mn ions in the ceramics. Surprisingly, the sharply enhanced ferromagnetism with $M_r = 0.4946 \text{ emu/g}$ and $M_s = 1.0298 \text{ emu/g}$ is obtained in the ceramic with $x = 7.0$, almost one thousand times larger than that of un-doped ceramic. The origin of the unusual ferromagnetism is associated with significant changes in magnetic orderings caused by Mn doping. The high magnetoelectric effect ($\alpha_{33} = 429.6 \text{ mV} \cdot \text{cm}^{-1} \cdot \text{Oe}^{-1}$) is obtained after the addition of 2.0 mol% Mn ions. Our study suggests that the present ceramics may have potential applications in advanced memory devices as promising lead-free high temperature piezoelectric and multiferroic materials.

1. Introduction

Lead-based perovskite piezoelectric ceramics (e.g., $\text{Pb}(\text{Ti,Zr})\text{O}_3$, $\text{BP}(\text{Mg}_{1/3}\text{Nb}_{2/3})\text{O}_3\text{-PbTiO}_3$, etc.) have been widely used in actuators, transformers and sensors due to their excellent piezoelectric properties near the morphotropic phase boundary (MPB).^{1,2} However, lead-based ceramics have serious harm to the human health and environment because of the strong toxicity of lead oxides. Therefore, there is a progressive demand for developing lead-free ferroelectric and piezoelectric ceramics. As promising candidates for lead-free materials, BaTiO_3 (BT)-,³ $\text{Bi}_{0.5}\text{Na}_{0.5}\text{TiO}_3$ (BNT)-⁴ and $\text{K}_{0.5}\text{Na}_{0.5}\text{NbO}_3$ (KNN)-based⁵ ceramics with good piezoelectric properties have been widely investigated. Unfortunately, these ceramics exhibit poor temperature stability, resulting from their low depolarization temperature, Curie temperature and/or the room-temperature coexistence of tetragonal and orthorhombic phases. Moreover, with the increasing development of electronic devices toward miniaturization, multiferroic materials which possess simultaneously two or more ferroic properties are of growing interest in recent years because of their potential application for new types of electronic devices.^{6,7} Therefore, it is urgent to develop new lead-free piezoelectric and multiferroic materials with considerable piezoelectricity, strong multiferrocity and good temperature stability of piezoelectric and ferroelectric properties.

Recently, BiFeO_3 (BFO) has become the focus of intense interest on single-phase multiferroic materials because of its particular multiferroicity at room temperature.⁸⁻¹⁰ BFO possesses a rhombohedral symmetry with a distorted perovskite structure at room temperature, a high Curie temperature ($T_C \sim 1103$ K) and G-type

antiferromagnetic Néel temperature ($T_N \sim 640$ K).^{11,12} This suggests that BFO has potential multifunctional applications in various advanced devices. However, two key factors have restricted macro-multiferroic nature of BFO:¹³⁻¹⁵ single-phase BFO is difficult to synthesis due to narrow temperature range of phase stabilization and thus some impurity phases are generally detected (e.g. $\text{Bi}_2\text{Fe}_4\text{O}_9$, $\text{Bi}_{25}\text{FeO}_{39}$, $\text{Bi}_{36}\text{Fe}_2\text{O}_{57}$, etc.); the reduction of Fe^{3+} to Fe^{2+} and formation of oxygen vacancies during sintering ($2\text{Fe}_{\text{Fe}} + \text{O}_{\text{O}} \rightarrow 2\text{Fe}'_{\text{Fe}} + \text{V}_{\text{O}}'' + \frac{1}{2}\text{O}_2$) lead to large leakage current in BFO materials. In order to improve the electric insulation and suppress the formation of impurity phases, many studies have been performed, including the use of various prepared techniques (e.g., chemical leaching, rapid liquid phase sintering, etc.),^{12,14} partial substitutions of analogous ions for Bi^{3+} or Fe^{3+} in the BFO lattices (e.g., Gd^{3+} , La^{3+} and Sm^{3+} for Bi^{3+} or Ga^{3+} , Al^{3+} and Co^{3+} for Fe^{3+})¹⁵⁻²⁰ and the formation of solid solutions of BFO with other ABO_3 -type perovskites (e.g., BaTiO_3 , CaTiO_3 , SrTiO_3 , $\text{Na}_{0.5}\text{Bi}_{0.5}\text{TiO}_3$ and $\text{K}_{0.5}\text{Na}_{0.5}\text{NbO}_3$).²¹⁻²⁷ Among these BFO-based solid solutions, BiFeO_3 - BaTiO_3 (BFO-BT) is a classic multiferroic material that has been intensively studied; however, these investigations mainly focused on dielectric and magnetic characteristics and rarely reported saturated ferroelectric hysteresis and strong piezoelectric response. In addition, there are no consensuses on the magnetic properties of BFO-BT solid solutions. For example, Kumar et al. reported linear magnetic hysteresis loops and antiferromagnetic nature of 0.75BFO-0.25BT ceramic,²⁸ while the same composition investigated by Futakuchi et al. shows a typical magnetic hysteresis loop and ferromagnetic moment with M_r of ~ 0.13 emu/g.²⁹ Our previous studies³⁰ show that

Sc-doped BiFeO₃-based ceramic, 0.725BiFe_{0.96}Sc_{0.04}O₃-0.275BaTiO₃, possesses improved piezoelectric and ferroelectric properties. On the other hand, it has been well known that as a frequently used dopant to tailor the electrical properties of piezoelectric materials, MnO₂ is one of the most interesting aids because of the multivalence states (Mn²⁺, Mn³⁺ and Mn⁴⁺) of Mn ions amongst many metal oxide dopants (e.g. La₂O₃, Nb₂O₅, MnO₂, Fe₂O₃, etc.). To our knowledge, there are few systematic reports on the effects of MnO₂ on the insulation, piezoelectric and multiferroic properties of BiFeO₃-based materials. In the present work, lead-free solid solutions of 0.725BiFe_{0.96}Sc_{0.04}O₃-0.275BaTiO₃-*x* mol% MnO₂ (BFS-BT-Mn-*x*) were synthesized by a conventional ceramic technique in air and the dominant roles of Mn-ions in improving insulation, piezoelectricity and multiferroicity of the ceramics were revealed. As a promising multiferroic and high-temperature piezoelectric candidate, this material exhibits large piezoelectricity, high Curie temperature, excellent temperature stability and strong multiferroicity, showing potential applications in multiferroic and high-temperature piezoelectric devices.

2. Experimental

0.725BiFe_{0.96}Sc_{0.04}O₃-0.275BaTiO₃-*x* mol%MnO₂ (BFS-BT-Mn-*x*) ceramics were fabricated by a conventional solid state reaction method using metal oxides and carbonate as powders: Bi₂O₃ (99.9%), Fe₂O₃ (99.0%), TiO₂ (98.0%), BaCO₃ (99.0%), Sc₂O₃ (99.9%) and MnO₂ (99.9%). All the raw materials in the stoichiometric ratio of

the $\text{BiFe}_{0.96}\text{Sc}_{0.04}\text{O}_3\text{-BaTiO}_3$ ceramics were first mixed thoroughly in ethanol using zirconia balls for 8 h, then dried and calcined at 800 °C for 4 h. After the calcination, MnO_2 was added. The resulting mixture was ball-milled again for 8 h, mixed thoroughly with a PVA binder solution and then pressed into disk samples. The samples were sintered at 950 °C for 2 h with a heating/cooling rate at 5 °C/min in the air. Silver electrode was co-fired on both surfaces of the sintered ceramics disks at 650 °C for 30 min. The samples were poled at 30-80 °C for 20 min and then cooled to room temperature in a silicone bath under a dc field of 2.0-5.0 kV/mm.

The crystalline structure of the sintered samples was determined using X-ray diffraction (XRD) analysis with $\text{Cu-K}\alpha$ ($\lambda = 1.540598 \text{ \AA}$) radiation (SmartLab, Rigaku), 0.01° scan step and continuous scanning type in the 2θ range of 20-70°. The microstructures were observed by scanning electron microscopy (FEI-Quanta 250, FEI). The composition analysis was recorded by a field-emission scanning electron microscope (JSM-7500), fitted out with energy dispersive spectroscopy (EDS). The average grain size D_A was obtained by multiplying the average linear intercept length of grains by 1.56.³¹ The relative permittivity ϵ_r at 1 MHz was measured as a function of temperature using a LCR meter (Agilent E4980A, Agilent Technologies Inc.) and temperature-controlled probe stage (Linkam TS1500E, Linkam Scientific Instruments Ltd). The polarization hysteresis (P - E , I - E) loops, leakage current density J and resistivity R were measured at room temperature using a precision materials measuring system (Premier II, Radiant Technologies Inc.). The X-ray photoelectron spectroscopy (XPS) spectra were measured using a PHI 5000 VersaProbe XPS

instrument (Thermo ESCALAB 250XI). The magnetic moments of the samples were measured using a superconducting quantum interferometric device SQUID magnetometer (Quantum Design) in the range of temperatures 4-400 K. Mössbauer spectroscopy using ^{57}Co as a radioactive source (OXFORD-MS-500) was carried out to investigate the magnetic ordering in the samples. The planar electromechanical coupling factor k_p was determined by the resonance method according to the IEEE Standard 176 using an impedance analyzer. The piezoelectric constant d_{33} was measured using a piezo- d_{33} meter (ZJ-3A, Institute of Acoustics). Magnetoelectric (ME) coefficient α_{33} was measured using a Helmholtz coil driven by a high-speed power amplifier (NF Electronic Instruments 4025). The values of α_{33} at different frequencies was calculated using

$$\alpha_{33} = \frac{dE_3}{dH_3}$$

where E_3 is the electric field generated in the thickness direction and H_3 is the applied ac magnetic field.

3. Results and discussions

Structural characterization

The XRD patterns of the BFS-BT-Mn- x ceramics sintered at 950 °C for 2 h are shown in Fig. 1. A pure perovskite phase can be observed in all the ceramics except for the composition of $x = 8.0$ with a small amount of non-magnetic impurities $\text{Bi}_2\text{Fe}_4\text{O}_9$. From Fig. 1b, the BFS-BT-Mn- x ceramics undergo gradually a structural transformation from rhombohedral to monoclinic phase with x increasing from 0 to

8.0, and thus a rhombohedral-monoclinic MPB is formed at $x = 0.5-1.0$. This is evidenced by the gradual change in the slope of the peaks near 39.0° and 45.5° . Similar to pure BFO, the ceramic with $x = 0$ possesses a rhombohedral symmetry. As x increases, the splitting of two diffraction peaks near 39° gradually becomes weak and merges into a single peak with x increasing from 0.0 to 1.0, and then splits into two peaks again with x further increasing from 2.0 to 8.0. Meanwhile, the (024) diffraction peak near 45.5° gradually splits into two peaks (021/220) with x increasing from 0 to 8.0. These suggest that the ceramics undergo the transformation from rhombohedral to monoclinic phase with x increasing from 0 to 8.0. It has been reported that MnO_2 can be converted into Mn_2O_3 at 650°C ($4\text{MnO}_2 \rightarrow 2\text{Mn}_2\text{O}_3 + \text{O}_2 \uparrow$), and the primary manganese ions are Mn^{3+} ions in the ceramics sintered at $960-990^\circ\text{C}$.³² However, for Mn-modified BFO-based materials, there is a reaction that can restrain the conversion of Fe^{3+} to Fe^{2+} between Mn^{3+} and Fe^{2+} :



and the spontaneity of this redox reaction is governed by the positive value of oxidation reduction potential (0.74 V).³² In the present work, all the samples were sintered at 950°C ; therefore, it can be reasonably inferred that the Mn ions exist in two valence states: Mn^{3+} with radius of 0.645\AA and Mn^{2+} with radius of 0.83\AA .³³ The ionic radius of Mn^{2+} and Mn^{3+} are much lower than that of Bi^{3+} (1.03\AA) and Ba^{2+} (1.35\AA), but very close to those of Fe^{3+} (0.645\AA), Ti^{4+} (0.605\AA) and Sc^{3+} (0.745\AA).³³ Therefore, according to the principles of crystal chemistry, Mn^{3+} and Mn^{2+} most

likely enter the B-sites for randomly substituting for Fe^{3+} , Ti^{4+} and Sc^{3+} ions due to their similar ionic radius (Fe/Ti/Sc ions vs. Mn ion). It can be also seen that all the diffraction peaks shift continuously toward lower 2θ in the ceramics with x increasing from 0.0 to 8.0, which should be attributed to the lattice expansion caused by the substitution of larger Mn ions ($\text{Mn}^{2+} \sim 0.83 \text{ \AA}$ and $\text{Mn}^{3+} \sim 0.645 \text{ \AA}$) for smaller B-sites cations ($\text{Fe}^{3+} \sim 0.645 \text{ \AA}$ and $\text{Ti}^{4+} \sim 0.605 \text{ \AA}$).³³

In order to characterize the phase transition, a general diffraction/reflectivity analysis program FULLPROF³⁵ was used to perform a full-pattern matching using the Rietveld method and refine structural parameters. Fig. 2 shows the XRD refinement of the BFS-BT-Mn- x ($x = 0, 2.0$ and 7.0) ceramics, and the corresponding refined structural parameters are shown in Table 1. Insets of Fig. 2 show the symmetric representation of the crystal structure of the BFS-BT-Mn- x ceramics with $x = 0, 2$ and 7 . From Fig. 2 and Table 1, for all the refinement, the final factors R_{wp} , R_{exp} and the goodness-of-fit indicator S (< 2.0) are 10.40%, 9.37% and 1.11 for BFS-BT-Mn-0, 11.40%, 5.82% and 1.96 for BFS-BT-Mn-2.0 and 12.80%, 6.84% and 1.87 for BFS-BT-Mn-7.0, respectively, indicating a good agreement matching between the observed and calculated patterns. For the ceramic with $x = 0$, the observed lattice parameters a , b , c and V are 5.6371 \AA , 5.6371 \AA , 13.8992 \AA and 382.5032 \AA^3 , respectively. The lattice parameters a , b , c and V clearly change to 5.6507 \AA , 5.6485 \AA , 3.9910 \AA and 127.3846 \AA^3 for the ceramic with $x = 2.0$, which remain a little change with those for the ceramic with $x = 7.0$. When the level of Mn ions is high, a part of Mn ions enter the lattices, while the others accumulate near the grain

boundaries (as shown in Fig. 4). As a result, the lattice constants remain a slight change in the ceramics with $x \geq 2.0$. Meanwhile, it can be noted that the atomic coordinates of the BFS-BT-Mn- x ($x = 2.0$ and 7.0) with monoclinic phase are obviously different from that of the un-doped ceramic with rhombohedral phase. These suggest that the internal structures of the ceramics have been transformed from rhombohedral to monoclinic phase with the increase of Mn ions.

Microstructural characterization

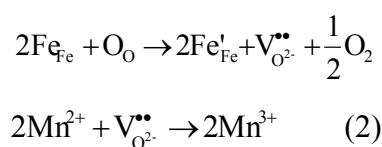
The SEM micrographs of the BFS-BT-Mn- x ($x = 0, 0.5, 1.0, 2.0, 4.0$ and 7.0) ceramics are shown in Fig. 3. It can be observed that the BFS-BT-Mn-0 has larger grain size ($3.49 \mu\text{m}$) than the ceramics with $x = 0, 0.5, 1.0, 2.0, 4.0$ and 7.0 ($2.75 \mu\text{m}$, $2.00 \mu\text{m}$, $0.86 \mu\text{m}$, $0.80 \mu\text{m}$ and $0.79 \mu\text{m}$, respectively), suggesting that the addition of Mn ions can significantly inhibit the grain growth because manganese oxide may accumulate near the grain boundaries and thus reduce the mobility of grain boundaries.³⁶ Similar effects of Mn doping on grain growth of the ceramics have been observed in Mn-doped $\text{Ba}_{0.85}\text{Ca}_{0.15}\text{Ti}_{0.90}\text{Zr}_{0.10}\text{O}_3$ ceramics.³⁷ In order to further confirm the chemical composition of these as-prepared ceramics, EDS has been taken at some selected positions of the BFS-BT-Mn-2.0 ceramic. Fig. 4 shows the composition analysis of (a) fracture, (b) a single small grain and a single large grain and (c) theoretical values of the ceramics with $x = 2.0$. From Figs. 4a and 4c, the ratio of all elements in whole regions containing all grains and grain boundaries is very close to the theoretical values, indicating that the chemical compositions are very average in

the ceramics. Fig. 4b shows the composition analysis of a single small grain and a single large grain in the BFS-BT-Mn-2.0 ceramics. It is observed that the Mn element is absent from the single small grain, whereas it can be detected in the single large grain and the whole region. These values of Mn element in different grains are lower than the theoretical value, suggesting that there is an inhomogeneous distribution of Mn element in grains. However, the average ratio of Mn element in whole regions is closed to the theoretical value. Therefore, it can be reasonably inferred that only a part of Mn ions enter into the grains, while there are still some Mn ions aggregated near the grain boundaries. It has been reported that the grain growth is inhibited and the grain size decreases when Mn aggregates at the grain boundary.³⁸

Chemical valence analysis

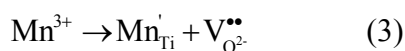
It is well known that for BFO perovskites, the chemical valence fluctuation is considerably sensitive to leakage current and multiferroic properties. To evaluate the valence states of the Fe and Mn ions, XPS for Bi 4*f*, O 1*s*, Fe 2*p* and Mn 2*p* core level binding energy spectra of the BFS-BT-Mn-*x* (*x* = 0, 0.5, 1.0, 2.0 and 7.0) ceramics are presented, and the peaks are fitted by Lorentzian-Gaussian functions as shown in Fig. 5. Fig. 5a shows the high resolution core spectra for Bi 4*f*. The two strongest peaks located at 158.75 eV and 164.05 eV correspond to Bi 4*f*_{7/2} and Bi 4*f*_{5/2}, and separation between the two peaks is 5.30 eV. These indicate that the bismuth element is present as stable Bi³⁺ ions in the ceramics. The high resolution core spectra for O 1*s* are shown in Fig. 5b. The high resolution core spectra of O 1*s* for the BFO-BT-Mn-*x* (*x* =

0, 2.0 and 7.0) ceramics can be decomposed into two peaks (one at ~531 eV and the other at ~529 eV). The former peak in binding energy located at 531.07 eV is ascribed to the intrinsic O^{2-} ions in the ceramics, meaning that the oxygen vacancy ($V_{O^{2-}}^{\bullet\bullet}$) exists in the sample. The peaks with lower binding energy correspond to the O 1s core spectra of the ceramics. By calculating the ratio of two fitted peaks, the concentration ratios of $V_{O^{2-}}^{\bullet\bullet}$ and O in the ceramics with $x = 0, 0.5, 1.0, 2.0$ and 7.0 are 53.28:46.72, 33.7:66.3, 44.3:55.7, 48.20:51.80 and 51.66:48.34, respectively. This indicates that as the content of Mn ions increases, the oxygen vacancies firstly decrease and then increases in Mn-modified BFS-BT ceramics. The high resolution core spectra for Fe 2p and Mn 2p of the BFS-BT-Mn- x ($x = 0, 0.5, 1.0, 2.0$ and 7.0) ceramics are shown in Figs. 5c and 5d, respectively. From Fig. 5c, the coexistence of Fe^{3+} and Fe^{2+} ions is observed in the ceramics. The ratios of Fe^{3+} and Fe^{2+} ions are 50.8:49.2, 53.5:46.5, 54.2:45.8, 54.6:45.4 and 56.6:43.4 for the ceramics with $x = 0, 0.5, 1.0, 2.0$ and 7.0 , respectively, indicating that the concentration of Fe^{2+} ions decreases gradually after Mn doping. Generally, less Fe^{2+} ions imply less oxygen vacancies,^{39,40} which can be described by the reaction equations (1) and (2). Moreover, with the valence fluctuation, there may be the following processes in the Mn-doped BFO-based ceramics.⁴¹ In this processes, $V_{O^{2-}}^{\bullet\bullet}$ will be as a bridge to maintain charge balance in BFO-based materials, which can be described by the following equations:



Therefore, the concentration of oxygen vacancies decreases after the addition of a

small amount of Mn ions doping. As expected, the leakage current density reduces. However, for the ceramics with $x > 0.5$, although the content of Fe^{2+} decreases with x increasing (i.e., the doping level of MnO_2), the concentration of oxygen vacancies increases, which leads to the degradation of the insulation of the materials. Clearly, there is a contradiction between $\text{V}_{\text{O}_2}^{\bullet\bullet}$ and Fe^{2+} in the ceramics with high levels of Mn doping. It can be inferred that the increase in oxygen vacancies of the ceramics with high levels of Mn cannot be attributed to the variation of valence states of Fe ions but should be attributed to the substitution of Mn ions for Fe^{3+} or Ti^{4+} ions. From Fig. 5d, as expected, there are no Mn 2p XPS spectra for the un-doped ceramic, while unlike the ceramic without MnO_2 doping, the characteristics of Mn 2p XPS spectra are partially observed in the ceramics with $x = 0.5$ and 1.0. For the ceramic with $x = 2.0$ and 7.0, the Mn 2p XPS spectra have been clearly observed and fitted. The peak observed at a binding energy of 641.0 eV corresponds to Mn^{2+} ions, while the strong peak located at 641.5 eV corresponds to Mn^{3+} ions. The fractions of $\text{Mn}^{2+}/\text{Mn}^{3+}$ ions in the ceramics with $x = 2.0$ and 7.0 were calculated to be 11%/89% and 14%/86%, respectively. This reveals the coexistence of Mn^{3+} and Mn^{2+} , which is similar to Mn-doped BFO materials.⁴² As mentioned above, Mn ions (Mn^{2+} and Mn^{3+}) can substitute B-site ions (Fe^{3+} and Ti^{4+}) due to their similar ionic radius (Fe/Ti/Sc ions vs. Mn ion). Thus, the addition of excess Mn ions leads to the formation of new oxygen vacancies (extrinsic oxygen vacancies)⁴¹ to maintain the charge neutrality:



where Mn'_{Ti} and Mn'_{Fe}/Mn''_{Ti} represent Mn^{3+} and Mn^{2+} , respectively, at the Ti/Fe sites. A large number of extrinsic oxygen vacancies are created by the substitutions of Mn ions for Fe^{3+} and Ti^{4+} ions because of excess Mn ions doping. Namely, when the content of MnO_2 increases, the extrinsic oxygen vacancies will be increased due to the substitution of Mn ions for B-sites cations, since there are more Mn^{2+} and Mn^{3+} ions in the vicinity of the Fe^{3+}/Ti^{4+} for the reaction between Mn^{3+} and Fe^{2+} in the ceramics with excess MnO_2 doping. Fe^{3+}/Ti^{4+} will be substituted mostly by Mn ions. Hence, the reactions (3) and (4) possess more advantages at high levels of Mn ions doping. Comparing the XPS spectra of O 1s with those of Fe 2p and Mn 2p, we can conclude that the level of Mn ions plays a decisive role in varying the oxygen vacancy of the present ceramics. The variation of the concentration of oxygen vacancies is probably determined by two competing factors: the oxidation of Mn^{3+} for Fe^{2+} and the substitution of Mn^{2+}/Mn^{3+} for Fe^{3+}/Ti^{4+} . Namely, the content of oxygen vacancies is determined by the competition effect between (1)-(2) and (3)-(4) equations. At low Mn ions levels, the reactions (1) and (2) play the dominant role; as a result, the concentration of oxygen vacancies decreases with x increasing. However, the reactions (3) and (4) possess more advantages at high Mn ions levels, which leads to the increase in the concentration of oxygen vacancies with x further increasing. Therefore, the ceramics exhibit low oxygen vacancy after the addition of a small amount of Mn ions. However, more oxygen vacancies originate from higher Mn ions doping level, leading to a continuous increase in leakage current (Fig. 6).

Electrical insulation

Large leakage current is a key factor to limit the application of BFO-based ceramics as piezoelectric/ferroelectric or multiferroic materials. Fig. 6a shows the leakage current density J of the BFS-BT-Mn- x ceramics with $x = 0, 0.5, 2.0$ and 7.0 sintered at $950\text{ }^{\circ}\text{C}$ for 2 h as a function of the electric field E , while Fig. 6b shows the dependence of the resistivity R of the BFS-BT-Mn- x ceramics under 3 kV/mm . From Fig. 6, the ceramic with $x = 0$ exhibits large leakage current density ($J = 1.2 \times 10^{-4}\text{ A/cm}^2$) and low resistivity ($R = 2.0 \times 10^8\ \Omega\cdot\text{cm}$). After the addition of 0.5 mol\% MnO_2 , the leakage current density and resistivity are $1.3 \times 10^{-6}\text{ A/cm}^2$ and $1.7 \times 10^{10}\ \Omega\cdot\text{cm}$, respectively, which have been almost improved by two orders of magnitude. However, the electrical insulation linearly degrades with x further increasing from 1.0 to 8.0 . From the results of the XPS, it can be concluded that the enhancement in the electric insulation may be ascribed to the suppression of the formation of $\text{Fe}_{\text{Fe}^{3+}}^{2+}$ and $\text{V}_{\text{O}^{2-}}^{\bullet\bullet}$ after a small amount of Mn doping ($x = 0.5$). However, with Mn ions further increasing from 1.0 to 8.0 , the concentration of oxygen vacancy notably increases due to the substitution of $\text{Mn}^{2+}/\text{Mn}^{3+}$ for $\text{Fe}^{3+}/\text{Ti}^{4+}$, leading to a continuous decrease in resistivity. Therefore, Mn ions play a decisive role on improving electrical in BFS-BT-Mn- x ceramics.

Ferroelectric properties

As well known, good electrical insulation is favorable to completely pole the ceramics; as a result, the large remanent polarization P_r may be easily obtained. For the ceramic with good insulation, it is difficult to cause a dielectric breakdown under

high electric field, and thus more possible polarization direction of ferroelectric domains can be changed under high electric field, which is beneficial for domains reversal. Therefore, the electrical insulation is the key factor to improve the ferroelectricity in BFO-based ceramics. In the present materials, saturated hysteresis loops are observed in the ceramics with low levels of MnO_2 . Fig. 7 shows the P - E (red line) and I - E (blue line) loops of the BFS-BT-Mn- x ceramics measured at room temperature and 10 Hz. As shown in Fig. 7a, the BFS-BT-Mn-0 ceramic exhibits a round and unsaturated P - E loop because of the poor electrical insulation. However, after the addition of 0.5-1.0 mol% MnO_2 , the BFS-BT-Mn- x ceramics exhibit typical and saturated P - E loops ($P_r = 13.1$ - $17.6 \mu\text{C}/\text{cm}^2$) due to the significantly increased resistivity (Fig. 6). With x further increasing from 2.0 to 8.0, the P - E loops become slim, slanted and then round, and the coercive field E_c decreases from 5.68 kV/mm to 3.73 kV/mm with x increasing from 0 to 2.0 and then increases generally with x further increasing to 8.0. These suggest that the ferroelectricity of the BFS-BT-Mn- x ceramics has a strong dependence on the MnO_2 doping level. The ferroelectricity is enhanced due to the improved insulation after a small amount of Mn ions doping ($x = 0.5$ - 1.0), whereas it is weakened because of the degraded insulation after the addition of excess Mn ions ($x \geq 2.0$). The increase in the coercive electric field of the ceramics with excess Mn ions doping may be attributed to MnO_2 as a “hard” dopant,³² namely when $\text{Mn}^{2+}/\text{Mn}^{3+}$ ions substitute for $\text{Fe}^{3+}/\text{Ti}^{4+}$, oxygen vacancies will be created. The appearance of the oxygen vacancies will lead to oxygen octahedral distortion, which will result in a pinning effect on domains reversal. On the other hand, the switching current curve allows the possibility of more precise evaluation of the coercive field by the current domain switching peak. For the ceramics with $x = 0$ - 1.0 (Figs. 7a-c), two obvious current peaks emerge, indicating that this ceramic experiences reversible electric-field-induced ferroelectric (FE) phase. The current peaks become weak until those disappear with x further increasing to 8.0, implying that the poor ferroelectric phase is obtained at excess Mn doping. Therefore, it can be concluded that the electrical insulation is the key factor to improve the ferroelectricity in Mn-doped BFS-BT ceramics.

From Figs. 7a, 7h-j, an interesting phenomenon can be noted that the resistivity of the ceramics with $x = 0, 6.0, 7.0$ and 8.0 possesses the same order of magnitude ($2.0 \times 10^8 - 6.5 \times 10^8 \Omega \cdot \text{cm}$). However, compared with the ceramic with $x = 0$, the BFS-BT-Mn- x ceramics with $x = 6.0, 7.0$ and 8.0 exhibit worse P - E loops and no apparent domain switching peaks. This indicates that the electrical insulation is not the only factor to determine the ferroelectric properties. The change in ferroelectricity may be implied to relate to the important role of Mn ions, which can be explained by the following two aspects. In the present ceramics, the electrical insulation decreases originating from the created oxygen vacancies by the substitution of $\text{Mn}^{2+}/\text{Mn}^{3+}$ for $\text{Fe}^{3+}/\text{Ti}^{4+}$. The appearance of the oxygen vacancies will lead to oxygen octahedral distortion. The oxygen vacancies result in a pinning effect on domains reversal. As a result, the ferroelectricity of the ceramic is weakened after the addition of the excess Mn ions. On the other hand, for ferroelectric perovskites, the materials with an unoccupied transition metal d orbital generally possess stable ferroelectric distortion.⁴³ Higuchi et al.³³ have proved that the Mn $3d$ electron of the majority- e_g orbital can transfer to the Fe $3d$ state through the Ti $3d$ orbital in BFO-BT ceramics. The appearance of occupied Ti $3d$ state weakens the stability of ferroelectric distortion, leading to the weakening of the ferroelectricity of the materials. Therefore, for the ceramics with $x = 0.05-1.0$, the insulation is greatly enhanced after the addition of a small amount of Mn ion (0.5-1.0 mol%), which makes the materials withstand high electric field and thus completely switches the ferroelectric domain and improves the ferroelectricity, while for the ceramics with $x > 1.0$, the decrease in both the insulation and the stability of ferroelectric distortion causes the degradation in ferroelectric properties of the ceramics with excess Mn ions doping ($x \geq 2.0$).

Fig. 8a shows the P - E loops of the BFS-BT-Mn-0.5 ceramic measured under an electric field of 8.5 kV/mm at different measuring temperatures, while Fig. 8b shows the temperature dependence on remanent P_r and coercive E_c for the BFS-BT-Mn-0.5 ceramic. From Fig. 8a, the BFS-BT-Mn-0.5 ceramic exhibits typical and saturated

P - E loops at different temperatures. The loops become slightly slimmer together with a reduction in E_c from 4.0 to 2.8 kV/mm with temperature increasing to 90 °C. As shown in Fig. 8b, the observed P_r increases slightly from 17.6 to 20.7 $\mu\text{C}/\text{cm}^2$ with temperature increasing from 20 to 90 °C. These indicate that the increase in temperature is a method to enhance the ferroelectric domain switching so as to obtain the low E_c and high P_r . Therefore, the large values of P_r can be obtained with increasing temperature. This shows that the BFS-BT-Mn-0.5 ceramic possesses good thermal stability of ferroelectric properties.

Dielectric properties

Fig. 9 shows the temperature dependences of the relative permittivity ϵ_r and loss tangent $\tan\delta$ at 1 MHz for the BFS-BT-Mn- x ceramics. From Fig. 9a, the BFS-BT-Mn-0 ceramic exhibits a sharp dielectric peak associated with the ferroelectric to paraelectric transition at 624 °C. As x increase from 0.5 to 1.0, the phase transition temperature slightly decreases from 596 °C to 590 °C, while the dielectric peaks gradually become broader due to the cation disorder (Fe^{3+} , Sc^{3+} , Ti^{4+} and $\text{Mn}^{2+/3+}$) in the ceramics. For the BFS-BT-Mn- x ceramics with $2.0 \leq x \leq 8.0$, two dielectric anomalies are obtained: one is associated with the ferroelectric-ferroelectric phase transition ($T_1 \sim 400\text{-}545$ °C) and the other is the ferroelectric-paraelectric phase transition ($T_2 \sim 650\text{-}725$ °C). The dielectric peaks at T_1 and T_2 gradually shift to lower temperature and the dielectric peak at T_1 becomes slightly weakened with x further increasing from 2.0 to 8.0. The appearance of two dielectric peaks may be related to

the structural characteristics of the phase transitions at T_1 and T_2 . Our previous studies⁴⁴ have shown that $\text{Bi}_{0.5}\text{K}_{0.5}\text{TiO}_3$ -modified BFO-BT ceramics with two phase transitions possess varied crystal structures with increasing temperature. It can be reasonably inferred that two phase transitions at T_1 (ferroelectric-ferroelectric) and T_2 (ferroelectric-paraelectric) may be related with the structural characteristics of the ceramic at different temperatures. From Fig. 9, relatively small $\tan\delta$ value ($\tan\delta < 0.9$) is observed up to 600 °C for all the ceramics. As temperature further increases, $\tan\delta$ increases dramatically, which may be attributed to poor electrical insulation at high temperature.

Piezoelectric properties

The composition dependence of d_{33} , k_p , ε_r and $\tan\delta$ for the BFS-BT-Mn- x ceramics is shown in Fig. 10. The BFS-BT-Mn-0 ceramic is difficult to be fully poled because of the considerably low resistivity and thus low d_{33} of ~30 pC/N is obtained. From Fig. 10a, the observed d_{33} dramatically increases from ~30 to 143 pC/N with x increasing from 0 to 0.5 and then decreases significantly from 123 to 2 pC/N with x further increasing from 1.0 to 8.0. The good piezoelectricity of the BFS-BT-Mn-1.0 ceramic should be attributed to the good electrical insulation and the formation of MPB: good electrical insulation is favorable to pole the ceramics while more possible polarization direction exists in the ceramics near the MPB. The observed k_p increases at first and then decreases with x increasing from 0 to 5.0, giving a maximum value of 0.35 at $x = 1.0$. The observed ε_r shows the similar trend, giving a maximum value of 557 at $x =$

0.5. The observed $\tan\delta$ decreases greatly from 80% to 2.8% with x increasing from 0 to 0.5 and then increases monotonically from 3.2% to 21.9% with x further increasing to 8.0. The variation of $\tan\delta$ with x is contrary to that of R (Fig. 6b).

Thermal stability of piezoelectric properties of ceramics is the decisive factor for high-temperature applications. It has been well known that poor temperature stability is always a key obstacle for the practical applications of lead-free piezoelectric ceramics. Here, the thermal-depolarization behavior (d_{33} , k_p and Q_m) and temperature dependence of ε_r at 1 MHz of the BFS-BT-Mn-0.5 ceramic sintered at 950 °C for 2 h is shown in Fig. 11a. The BFS-BT-Mn-0.5 ceramic was annealed at selected temperature for 1 h, and then its d_{33} was re-measured at room temperature. The results in Fig. 11; show that the BFS-BT-Mn-0.5 ceramic with good piezoelectricity possesses the excellent thermal stability of d_{33} , which should be attributed to the high T_d of 425 °C and T_C of 596 °C. The observed d_{33} decreases slightly from 143 to 109 pC/N with annealing temperature increasing from 25 °C to 425 °C. As the annealing temperature further increases to 475 °C, the observed d_{33} greatly decreases to 42 pC/N. However, at the annealing temperatures of 475-550 °C, the observed d_{33} almost remains unchanged at ~40 pC/N. Finally, as the annealing temperature increases to 675 °C, the observed d_{33} sharply decreases to 4 pC/N. The variation of k_p and Q_m is consistent with that of d_{33} . Obviously, the depolarization of the ceramic occurs at the considerably wide temperature range (425-675 °C), exhibits a two-step depolarization behavior (425-475 °C and 575-675 °C, respectively) and shows an interesting plateau

(475-575 °C). This phenomenon may be associated with compositional fluctuations. Yabuta et al. have confirmed that BFO- and BT-rich compositions exist in the BFO-BT ceramics.⁴⁵ Therefore, it can be reasonably inferred that there are BT- and BFO-rich microdomains in some grains of the Mn-doped BFS-BT ceramics, and thus the depolarization behavior of the BFS-BT-Mn-0.5 ceramic is divided into two steps by a plateau. Similar two-step depolarization behavior has been observed in the Bi_{0.5}K_{0.5}TiO₃-modified BiFeO₃-BaTiO₃ ceramics.⁴⁴

The depolarization behavior of the ceramics may be related to the nature of phase transition at high temperature. In general, the compositional fluctuations in perovskite ferroelectrics lead to the diffusive phase transition. The diffuseness of the phase transition can be obtained from the modified Curie-Weiss law $1/\varepsilon - 1/\varepsilon_m = C^{-1}(T - T_m)^\gamma$,^{30,46} where ε_m is the maximum value of ε_r at the phase transition temperature T_m , γ is the degree of diffuseness, and C is the Curie-like constant. The value of γ ranges from 1 for a normal ferroelectric to 2 for an ideal relaxor ferroelectric. By fitting the experimental data to the equation, the γ value can be obtained. The inset of Fig. 11a shows the curve of $\ln(1/\varepsilon - 1/\varepsilon_m)$ as a function of $\ln(T - T_m)$ for the BFS-BT-Mn-0.5 ceramic at 1 MHz. It can be seen that the observed γ (1.49) is far greater than 1, indicating that the phase transition is diffusive. Therefore, the depolarization behavior of the BFS-BT-Mn-0.5 ceramic may be related to the diffusive characteristic of ferroelectric-paraelectric phase transition at T_C . In addition, it should be noted that the BFS-BT-Mn-0.5 ceramic still gives weak piezoelectric response ($d_{33} \sim 2.0$ pC/N) even if the annealing temperature exceeds the Curie

temperature ($T_C = 596\text{ }^\circ\text{C}$), which may be attributed to the diffusive ferroelectric-paraelectric phase transition.

Figs. 11b and 11c show the relationships between the piezoelectric constant d_{33} and Curie temperature T_C /depolarization temperature T_d for the lead-based and lead-free piezoelectric materials. The corresponding d_{33} , T_C and T_d of these ceramics are listed in Table 2. From the Figs. 11b, 11c and Table 2, the lead-based materials possess high d_{33} of $\sim 350\text{ pC/N}$, however, the relatively low T_C of $420\text{ }^\circ\text{C}$ and T_d of $320\text{ }^\circ\text{C}$ would limit the application at high temperatures.^{47,48} As for lead-free ceramics, the Aurivillius bismuth oxide layer-structure ferroelectrics (BLSFs) exhibit high T_C ($655\text{-}939\text{ }^\circ\text{C}$) and T_d ($500\text{-}900\text{ }^\circ\text{C}$), but the issue of low d_{33} ($11.5\text{-}28\text{ pC/N}$) has not been effectively solved, originating from high E_c and two-dimensional orientation restriction of the rotation of spontaneous polarization in the BLSFs materials.⁴⁹⁻⁵¹ In addition, as promising candidates for lead-free materials, KNN-,^{52,53} BNT-,^{54,55} and BT-based^{56,57} materials commonly exhibit good piezoelectric properties. Unfortunately, these ceramics generally exhibit poor temperature stability induced by the low T_d ($70\text{-}300\text{ }^\circ\text{C}$), T_C and/or the room-temperature coexistence of tetragonal and orthorhombic phases. Compared with the above materials, BFO-based ceramics⁵⁸⁻⁶¹ are much attractive candidates for being the high-temperature piezoelectric ceramics due to their super high T_C/T_d and large d_{33} . It can be seen that the BFO-based ceramics simultaneously show high d_{33} ($136\text{-}163\text{ pC/N}$) and high T_C/T_d ($428\text{-}485\text{ }^\circ\text{C}/380\text{-}425\text{ }^\circ\text{C}$). In this study, the BFS-BT-Mn-0.5 ceramic shows much higher T_C of $596\text{ }^\circ\text{C}$ and T_d of $425\text{ }^\circ\text{C}$ than those for Pb-, BT-, BNT- and KNN-based materials, along with the

relatively large d_{33} of 143 pC/N, suggesting the BFS-BT-Mn-0.5 ceramic has promising applications in high-temperature piezoelectric devices.

Magnetic Properties

Fig. 12a shows the M - H hysteresis loops of the BFS-BT-Mn- x ceramics, while Fig. 12b shows composition dependence of remanent magnetization M_r , saturation magnetization M_s and coercivity H_c . As a composition, pure BFO has been synthesized and its M - H loop is shown in the inset of Fig. 12a. It can be seen that the pure BFO exhibits a linear magnetic field dependence of magnetization indicative of its antiferromagnetic (AFM) nature, which is consistent with the literature.⁶² Similar characteristic is observed in the BFS-BT-Mn-0 ceramic, indicating that the un-doped ceramic exhibits mainly AFM ordering. The observed M_r of 3.8×10^{-4} emu/g and M_s of 9×10^{-4} emu/g are obtained in the ceramic without Mn doping. After the addition of MnO_2 , the ceramics exhibit the typical magnetization hysteresis loop. Obviously, from Fig. 12b, it can be seen that the magnetism of the ceramics is greatly enhanced after the addition of 1.0-7.0 mol% MnO_2 , and the observed M_r and M_s give maximum values of 0.4946 emu/g and 1.0298 emu/g at $x = 7.0$, respectively. However, the slight decrease in the magnetism ($M_r = 0.4880$ emu/g and $M_s = 0.9938$ emu/g) is obtained in the BFS-BT-Mn-8.0 ceramic. The observed H_c increases initially from 0.15 kOe to 1.5 kOe with x increasing from 0 to 4.0 and then retains a constant with x further increasing. For the present ceramics, the change in magnetization can be explained in the following. On the one hand, the ferromagnetism has been reported to be more

dependent on structural distortions.⁶³ In this work, when $\text{Mn}^{3+/2+}$ substitutes for Fe^{3+} or Ti^{4+} , the Jahn-Teller effect occurs.⁶⁴ Namely when $\text{Mn}^{3+/2+}$ ions enter an oxygen octahedron, the lattices around the $\text{Mn}^{3+/2+}$ distorts, resulting in the symmetry of the crystal structure and breaking the local spin helix structure of BFO. Therefore, M_r and M_s of the ceramics increase continuously with x increasing from 0 to 7.0. On the other hand, it has been noted that the statistical distribution of Sc^{3+} , Fe^{3+} and Ti^{4+} ions in the octahedral spaces and the creation of lattice defects lead to the bulk magnetization and ferromagnetism.⁶⁵ For the present ceramics, $\text{Mn}^{2+/3+}$, Fe^{3+} , Ti^{4+} , Sc^{3+} occupy statistically the B-sites of the ceramics; in addition, the $\text{Mn}^{2+}/\text{Mn}^{3+}$ can enter the crystal lattices to substitute for Fe^{3+} or Ti^{4+} , which would induce lattice defects. Hence the magnetism of the ceramics increases with the addition of 1.0-7.0 mol% Mn ions. However, excess Mn ions ($x = 8.0$) weakens the magnetism of the ceramic because of the formation of nonmagnetic impurities $\text{Bi}_2\text{Fe}_2\text{O}_9$ (Fig. 1). It can be concluded that Mn ions doping has a greatly positive influence on the ferromagnetism of BFO-based ceramics.

The temperature dependence on magnetization ($M-T$) of the ceramics with $x = 0$, 2.0 and 7.0 were measured in both zero-field-cooled (ZFC) and field-cooled (FC) modes at $H = 1.0$ kOe and the results are shown in Fig. 13. From Fig. 13a, both ZFC and FC curves of BFS-BT-Mn-0 ceramic exhibit nonlinear increase with the temperature decreasing from 400 K to 8 K, indicating that the ceramic presents mostly AFM ordering at this temperature range. This result is consistent with the analysis of

M-H loop (Fig. 12). After the addition of 2.0 mol% and 7.0 mol% MnO_2 , the ceramics exhibit completely different ZFC and FC curves. As the temperature increases, the clear AFM to paramagnetic (PM) transitions of the ceramics with $x = 2.0$ and 7.0 are obtained at ~ 110 K and ~ 155 K, respectively. As well known, pure BFO is classified as AFM with the Néel temperature $T_N \sim 640$ K. In addition, Buscaglia et al. have confirmed that the presence of the non-magnetic BaTiO_3 phase causes a reduction of Néel temperature in BFO-BT materials.⁶⁶ Therefore, it can be reasonably inferred that the un-doped BFS-BT ceramic may exhibit low T_N (~ 400 K) than pure BFO. The ceramics with $x = 2.0$ and 7.0 show lower T_N than room temperature, which should be associated with the effect of Mn ions doping. Further research is needed to reveal the role of Mn ions in present ceramics. Moreover, the divergence between ZFC and FC magnetization curves is similar to that found for other ferro- and ferromagnetic materials⁶⁷, indicating that the sample is ferromagnetic. The divergence increases with the Mn ions doping, implying that the ferromagnetic properties of the ceramic are enhanced. Therefore, the increase in magnetic transition (AFM to PM) and improved ferromagnetic properties can be simultaneously achieved in these ceramics.

Fig. 14 shows the Mössbauer spectra on the ^{57}Fe nuclei for the BFS-BT-Mn- x ($x = 0, 2.0$ and 7.0) ceramics at room temperature using ^{57}Co as a radioactive source. The red lines give least-square fits of the experimental spectra to theoretical spectra, assuming from Lorentzian absorption line shapes and a distribution of magnetic hyperfine fields. From Fig. 14a, the Mössbauer spectrum of un-doped BFS-BT

ceramic shows a characteristic asymmetry, which is similar to that of the reported BFO-BT ceramics.⁶⁸ The spectrum shows a magnetic spectral signature which corresponds to high spin ferric ions in different crystallographic environments at dissimilar electric field gradients. The best numerical fitting of our experimental data to theoretical spectra gives values of the isomer shift of $\delta_1 = 0.38$ mm/s and $\delta_2 = 0.36$ mm/s, quadruple splitting of $Q_s = 0.05$ mm/s and 0.03 mm/s and magnetic hyperfine field of $B_{hf} = 397$ kOe and $B_{hf} = 359$ kOe, respectively. With x increasing, the spectra become broadened, which is ascribed to the nature of disorder in the superexchange magnetic interaction paths resulting from the random substitution of Fe^{3+} ions by the magnetic $\text{Mn}^{2+}/\text{Mn}^{3+}$ and non- magnetic $\text{Ti}^{4+}/\text{Sc}^{3+}$ ions in the structure of BFS-BT. Concomitantly, the overall splitting of the outer magnetic absorption lines that measures the average effective magnetic hyperfine field at the nucleus decreases, reflecting the weakening of the inherent strength of the magnetic interactions 74. Specifically, from Figs. 14b and 14c, we obtain the B_{hf} values of 306 kOe for $x = 2.0$, and 222 kOe for $x = 7.0$, respectively. Therefore, the overall spectral characteristics indicate the formation of solid solution phases and a gradual magnetic phase transformation from a relatively well-ordered spin structure for the BFS-BT-Mn-0 ceramic to an increasing spin disordered magnetic phase for the ceramics with Mn ions doping. Our results are in good agreement with the improved ferromagnetism and the change in magnetic orderings as shown in Fig. 12 and Fig. 13.

The ME effect is a product property of multiferroic materials. Fig. 16 shows the

frequency dependence of α_{33} of the BFS-BT-Mn- x ceramics with $x = 0, 2.0$ and 7.0 . For the ceramic with $x = 0$, the α_{33} increases linearly with frequency increasing from 10 to 350 kHz. The observed α_{33} is small, which may be attributed to the poor magnetic properties (Fig. 12). After the addition of 2 mol% Mn ions, the ceramic exhibits a large α_{33} of as high as $429.57 \text{ mV}\cdot\text{cm}^{-1}\cdot\text{Oe}^{-1}$ at resonant frequency of 257 kHz. This improvement in ME effect may be attributed to the enhanced resistivity ($R \sim 7.9 \times 10^9 \Omega\cdot\text{cm}$), ferroelectricity ($P_r = 8.7 \mu\text{C}/\text{cm}^2$) and ferromagnetism ($M_r = 0.059 \text{ emu/g}$) of the BFS-BT-Mn- x ceramic at $x = 2.0$ (Figs. 6, 7 and 12). As x further increases ($x = 7.0$), the observed α_{33} increases monotonically with frequency because of the reduced resistivity and the difficult reversal of the ferroelectric domain (Figs. 6 and 7). Besides the resonance ME effect, even without a DC bias magnetic field, the samples still exhibit reasonably high α_{33} at low frequency when compared to the reported values of lead-free ME materials such as $\text{Bi}_{0.7}(\text{Ba,Sr})_{0.3}\text{FeO}_3$ ($2.1 \text{ mV}\cdot\text{cm}^{-1}\cdot\text{Oe}^{-1}$)⁶⁹ and BFO ($3.0 \text{ mV}\cdot\text{cm}^{-1}\cdot\text{Oe}^{-1}$).⁷⁰ The results indicate that the ME performance of the ceramic could be enhanced significantly after the addition 2.0 mol% Mn ions. These show that the ceramics with considerable piezoelectric and ME performance have a potential application in multiferroic devices.

4. Conclusion

New lead-free multiferroic ceramics of $\text{BiFe}_{0.96}\text{Sc}_{0.04}\text{O}_3\text{-BaTiO}_3\text{-Mn-}x$ have been successfully fabricated by a conventional ceramic technique, and the effects of Mn

doping on phase structure, multiferroic and piezoelectric properties of the ceramics have been studied. All the ceramics sintered at low sintering temperature of 950 °C for 2 h possess a perovskite structure, and a morphotropic phase boundary (MPB) of rhombohedral and monoclinic phases is formed at $x = 0.5-1.0$. The ceramics located within MPB exhibit high electric insulation, good piezoelectricity, strong ferroelectricity, high Curie temperature and excellent temperature stability of piezoelectric and ferroelectric properties. These behaviors are greatly associated with the contribution of Mn ions in the ceramics. The sharply enhanced ferromagnetism with $M_r = 0.4946$ emu/g and $M_s = 1.0298$ emu/g is obtained in the ceramic with $x = 7.0$ at room temperature, almost one thousand times as much as that of un-doped ceramic. The high ME effect ($\alpha_{33} = 429.6$ mV·cm⁻¹·Oe⁻¹) is obtained after the addition 2.0 mol% Mn ions. The present work provides an alternative way for improving multiferroic properties of BiFeO₃-based materials, while the present ceramics may have potential applications in advanced memory devices as promising lead-free high piezoelectric and multiferroic materials.

Acknowledgements

This work was supported by the projects of Education Department of Sichuan Province (15ZA0037 and 15ZB0032), Science and Technology Bureau of Sichuan Province (2014JY0040).

References

- 1 B. Jaffe, W. R. Cook and H. Jaffe, *Piezoelectric Ceramics*, Academic, London, 1971.
- 2 F. Gao, R. Hong, J. Liu, Z. Li, L. Cheng and C. Tian, *J. Alloys Compd.*, 2009, **475**, 619-623.
- 3 W. Liu and X. Ren, *Phys. Rev. Lett.*, 2009, **103**, 257602.
- 4 C. Xu, D. Lin and K. W. Kwok, *Solid State Sci.*, 2008, **10**, 934-940.
- 5 R. Zuo, J. Rodel, R. Chen and L. Li, *J. Am. Ceram. Soc.*, 2006, **89**, 2010-2014.
- 6 M. Fiebig, *J. Phys. D: Appl. Phys.*, 2005, **38**, R123-152.
- 7 G. Catalan and J. F. Scott, *Adv. Mater.*, 2009, **21**, 2463.
- 8 S. H. Baek, C. M. Folkman, J. W. Park, L. Sanghan, W. B. Chung, T. Tomas and B. Chang, *Adv. Mater.*, 2011, **23**, 1621-1625.
- 9 H. Singh, A. Kumar and K. L. Yadav, *Mater. Sci. Eng. B*, 2011, **176**, 540-547.
- 10 J. M. Moreau, C. Michel, R. Gerson and W. J. James, *J. Phys. Chem. Solids*, 1971, **32**, 1315-1320.
- 11 G. A. Smolenskii and I. E. Chupis, *Sov. Phys. Usp.*, 1982, **25**, 475.
- 12 A. K. Pradhan, K. Zhang, D. Hunter, J. B. Dadson and G. B. Loutts, *J. Appl. Phys.* 2005, **97**, 093903.
- 13 S. K. Pradhann and B. K. Roul, *Physica B*, 2011, **406**, 3313.
- 14 M. M. Kumar, V. R. Palkar, K. Srinivas and S. V. Suryanarayana, *Appl. Phys. Lett.*, 2000, **76**, 2764.
- 15 Q. Zhang, X. H. Zhu, Y. H. Xu, H. B. Gao, Y. J. Xiao, D. Y. Liang, J. L. Zhu, J. G. Zhu and D. Q. Xiao, *J. Alloys Compd.*, 2013, **546**, 57-62.

- 16 S. Pattanayak, R. N. P. Choudhary, S. R. Shannigrahi, P. R. Das and R. Padhee, *J. Magn. Magn. Mater.*, 2013, **341**, 158-164.
- 17 X. M. Chen, J. L. Wang, G. L. Yuan, D. Wu, J. M. Liu, J. Yin and Z. G. Liu, *J. Alloys Compd.*, 2012, **541**, 173-176.
- 18 W. Dong, Y. P. Guo, B. Guo, H. Y. Liu, H. Li and H. Z. Liu, *Mater. Lett.*, 2013, **91**, 359-361.
- 19 F. Roulland, C. Lefevre, A. Thomasson and N. Viart, *J. Eur. Ceram. Soc.*, 2013, **33**, 1029-1035.
- 20 X. J. Xi, S. Y. Wang, W. F. Liu, H. J. Wang, F. Guo, X. Wang, J. Gao and D. J. Li, *J. Magn. Magn. Mater.*, 2014, **355**, 259-264.
- 21 H. L. Zhang, W. Jo, K. Wang and K. G. Webber, *Ceram. Int.*, 2014, **40**, 4759-4765.
- 22 T. H. Wang, C. S. Tu, Y. Ding, T. C. Lin, C. S. Ku, W. C. Yang, H. H. Yu, K. T. Wu, Y. D. Yao and H. Y. Lee, *Curr. Appl Phys.*, 2011, **11**, S240-S243.
- 23 Y. X. Wei, X. T. Wang, J. T. Zhu, X. L. Wang and J. J. Jia, *J. Am. Ceram. Soc.*, 2013, **96**, 1-6.
- 24 Q. Q. Wang, Z. Wang, X. Q. Liu and X. M. Chen, *J. Am. Ceram. Soc.*, 2012, **95**, 670-675.
- 25 Z. Z. Ma, Z. M. Tian, J. Q. Li, C. H. Wang, S. X. Huo, H. N. Duan and S. L. Yuan, *Solid State Sci.*, 2011, **13**, 2196-2200.
- 26 H. Y. Liu, Y. P. Guo, B. Guo, W. Dong and D. Zhang, *J. Eur. Ceram. Soc.*, 2012, **32**, 4335-4340.
- 27 S. X. Huo, S. L. Yuan, Y. Qiu, Z. Z. Ma and C. H. Wang, *Mater. Lett.*, 2012, **68**, 8-10.

- 28 M.M. Kumar, A. Srinivas, G. S. Kumar and S. V. Suryanarayana, *J. Phys. Condens. Matter*, 1999, **11**, 8131-8139.
- 29 T. Futakuchi, T. Kakuda and Y. Sakal, *J. Ceram. Soc. Jpn.*, 2014, **122**, 464-468.
- 30 Y. Wan, Y. Li, Q. Li, W. Zhou, Q. J. Zheng, X. C. Wu, C. G. Xu, B. P. Zhu and D. M. Lin, *J. Am. Ceram. Soc.*, 2014, **97**, 1809-1818.
- 31 M. I. Mendelson, *J. Am. Ceram. Soc.*, 1968, **52**, 443-446.
- 32 X. H. Liu, Z. Xu, S. B. Qu, X. Y. Wei and J. L. Chen, *Ceram. Int.*, 2008, **34**, 797-801.
- 33 T. Higuchi, W. Sakamoto, N. Itoh, T. Shimura, T. Hattori and T. Yogo, *Appl. Phys. Express*, 2008, **1**, 011502.
- 34 J. Wang, Z. Fu, R. Peng, M. Liu, S. Sun, H. Huang, L. Li, R.J. Knize and Y. Lu, *Mater. Horiz.*, 2015, **2**, 232-236.
- 35 J. Rodriguez-Carvajal, Recent Developments of the Program FULLPROF. In *CPD Newsletter* 2001, Vol. 26, P 12; available at <http://www.ill.eu/sites/fullprof/index.html>.
- 36 Y. Hou, M. Zhu, F. Gao, H. Wang, B. Wang, H. Yan and C. Tian, *J. Am. Ceram. Soc.*, 2004, **87**, 847.
- 37 M. Jiang, Q. Lin, D. Lin, Q. Zheng, X. Fan, X. Wu, H. Sun, Y. Wan and L. Wu, *J. Mater. Sci.*, 2013, **48**, 1035-1041.
- 38 H. Zhang, H. Deng, C. Chen, L. Li, D. Lin, X. Li, X. Zhao, H. Luo and J. Yan, *Scr. Mater.*, 2014, **75**, 50-53.
- 39 J. Wu, B. Zhang, X. Wang, J. Wang, J. Zhu and D. Xiao, *Mater. Res. Bull.*, 2013, **48**, 2973-2977.

- 40 G. Dong, G. Tan, Y. Luo, W. Liu, A. Xia and H. Ren, *Appl. Surf. Sci.* 2014, **305**, 55–61.
- 41 L. Liu, R. Zuo and Q. Liang, *Appl. Surf. Sci.*, 2013, **268**, 327-331.
- 42 S. W. Kim and W. J. Kim, *J. Korean Phys. Soc.*, 2013, **63**, 2325-2329.
- 43 G. L. Yuan, S. W. Or, J. M. Liu and Z. G. Liu, *Appl. Phys. Lett.*, 2006, **89**, 052905.
- 44 D. Lin, Q. Zheng, Y. Li, Y. Wan, Q. Li and W. Zhou, *J. Eur. Ceram. Soc.*, 2013, **33**, 3023.
- 45 H. Yabuta, M. Shimada, T. Watanabe, J. Hayashi, M. Kubota, K. Miura, T. Fukui, I. Fujii and S. Wada, *Jpn. J. Appl. Phys.*, 2012, **51**, 09LD04.
- 46 K. Uchino, S. Nomura, L. E. Cross, S. J. Tang and R. E. Newnham, *J. Appl. Phys.*, 1980, **51**, 1142.
- 47 X. Chao, Z. Yang, L. Xiong and Z. Li, *J. Alloys Compd.*, 2011, **509**, 512-517.
- 48 Q. Liao, S. Chen, X. Chu, F. Zeng and D. Guo, *Sens. Actuator A*, 2013, **201**, 222-229.
- 49 D. Gao, K. W. Kwok and D. Lin, *Curr. Appl Phys.*, 2011, **11**, S124-S127.
- 50 Z. Peng, Q. Chen, Y. Wang, D. Xin, D. Xiao and J. Zhu, *Mater. Lett.*, 2013, **107**, 14-16.
- 51 H. Chen and J. Zhai, *Int. J. Appl. Ceram. Technol.*, 2013, **10**, E151-E158.
- 52 X. Wang, J. Wu, X. Cheng, B. Zhang, D. Xiao, J. Zhu, J. Wang and X. Lou, *J. Phys. D: Appl. Phys.*, 2013, **46**, 495305.
- 53 D. Lin, K. W. Kwok and H. L. W. Chan, *J. Appl. Phys.*, 2007, **102**, 034102.
- 54 C. Xu, D. Lin and K. W. Kwok, *Solid State Sci.*, 2008, **10**, 934-940.

- 55 D. Lin, C. Xu, Q. Zheng, Y. Wei and D. Gao, *J. Mater. Sci. - Mater. Electron.*, 2009, **20**, 393-397
- 56 S. Su, R. Zuo, S. Lu, Z. Xu, X. Wang, and L. Li, *Curr. Appl Phys.*, 2011, **11**, S120-S123.
- 57 W. Lin, L. Fan, D. Lin, Q. Zheng, X. Fan and H. Sun, *Curr. Appl Phys.*, 2013, **13**, 159-164.
- 58 H. Yang, C. Zhou, X. Liu, Q. Zhou, G. Chen, H. Wang and W. Li, *Mater. Res. Bull.*, 2012, **47**, 4233-4239.
- 59 X. Shan, C. Zhou, Z. Cen, H. Yang, Q. Zhou and W. Li, *Ceram. Int.*, 2013, **39**, 6707-6712.
- 60 Z. Cen, Z. Zhou, J. Cheng, X. Zhou, W. Li, C. Yan, S. Feng, Y. Liu and D. Lao, *J. Alloys Compd.*, 2013, **567**, 110-114.
- 61 X. Zhou, C. Zhou, Q. Zhou, H. Yang, Z. Cen, J. Cheng, L. Cao and Q. Fan, *J. Electron. Mater.*, 2014, **43**, 755-760.
- 62 D. Lebeugle, D. Colson, A. Forget, M. Viret, A. M. Bataille and A. Gukasov, *Phys. Rev. Lett.*, 2008, **100**, 227602.
- 63 M. M. Kumar, S. Srinath, G. S. Kumar and S. V. Suryanarayana, *J. Magn. Magn. Mater.*, 1998, **188**, 203-212.
- 64 W. L. Zhong, *Physics of Ferroelectrics*, Science Press. Beijing, 2000, 430-433.
- 65 G. A. Gehring, *Ferroelectrics*, 1994, **161**, 275-285.
- 66 M. T. Buscaglia, L. Mitoseriu, V. Buscaglia, I. Pallecchi, M. Viviani, P. Nanni and A. Siri, *J. Eur. Ceram. Soc.*, 2006, **26**, 3027-3030.

- 67 P. A. Joy and S. K. Date, *J. Magn. Magn. Mater.*, 2000, **218**, 229.
- 68 K. Kowal, E. Jartych, P. Guzdek, P. Stoch, B. Wodecka-Duś, A. Lisińska-Czekaj and D. Czekaj, *Nukleonika*, 2013, **58**, 57-61.
- 69 V. B. Naik and R. Mahendiran, *Solid State Commun.*, 2009, **149**, 754-758.
- 70 J. M. Caicedo, J. A. Zapata and M. E. Gomez, P. Prieto, *J. Appl. Phys.*, 2008, **103**, 07E306-07E308.

Table captions

Table 1 Refined structural parameters of BFS-BT-Mn-x (x = 0, 2.0 and 7.0)

Table 2 d_{33} , T_C and T_d of the piezoelectric ceramics.

Figure captions

Fig. 1 XRD patterns of the BFS-BT-Mn- x ceramics sintered at 950 °C for 2 h in the 2θ range of (a) 20-70° and (b) 38-47°.

Fig. 2 XRD refinement of the BFS-BT-Mn- x ($x = 0, 2.0$ and 7.0) ceramics.

Fig. 3 SEM micrographs of the BFS-BT-Mn- x ceramics: (a) $x = 0$, (b) $x = 0.5$, (c) $x = 1.0$ (d) $x = 2.0$, (e) $x = 4.0$ and (f) $x = 7.0$.

Fig. 4 Composition analysis of (a) fracture section, (b) a single small grain and a single large grain and (c) theoretical values of the BFS-BT-Mn-2.0 ceramics.

Fig. 5 (Color online) XPS fitting for (a) Bi, (b) O, (c) Fe and (d) Mn elements of the BFS-BT-Mn- x ($x = 0, 0.5, 1.0, 2.0, 7.0$) ceramics.

Fig. 6 (a) Leakage current density J of the BFS-BT-Mn- x ceramics at room temperature as a function of the electric field E ; (b) dependence of resistivity R of the BFS-BT-Mn- x ceramics on x under 3 kV/mm.

Fig. 7 P - E (red line) and I - E (blue line) loops of the BFS-BT-Mn- x ceramics measured at room temperature and 10 Hz.

Fig. 8 (a) P - E loops of the BFS-BT-Mn-0.5 ceramic at different temperatures; (b) temperature dependence on P_r and E_c for the BFS-BT-Mn-0.5 ceramic.

Fig. 9 Temperature dependence of relative permittivity ϵ_r and loss tangent $\tan\delta$ at 1 MHz for the BFS-BT-Mn- x ceramics.

Fig. 10 Composition dependence of (a) d_{33} , k_p , (b) ϵ_r and $\tan\delta$ of the BFS-BT-Mn- x ceramics.

Fig. 11 (a) Thermal-depoling behavior and temperature dependence of ε_r at 1 MHz of the BFS-BT-Mn-0.5 ceramic (inset: plot of $\ln(1/\varepsilon_r - 1/\varepsilon_m)$ versus $\ln(T - T_m)$); (b) and (c) relationships between d_{33} and Curie temperature T_C /depolarization temperature T_d for the reported piezoelectric materials.

Fig. 12 (a) $M-H$ loops of the BFS-BT-Mn- x ceramics at room temperature (the inset is $M-H$ of the pure BiFeO₃ ceramic sintered at 775 °C for 2 h and the BFS-BT-Mn-0 ceramic), (b) composition dependence of remanent magnetization M_r , saturation magnetization M_s and coercivity H_c .

Fig. 13 ZFC and FC curves of the BFS-BT-Mn- x ceramics with (a) $x = 0$, (b) $x = 2.0$ and (c) $x = 7.0$.

Fig. 14 Mössbauer spectra on the ⁵⁷Fe nuclei in the BFS-BT-Mn- x ceramics at room temperature; (a) $x = 0$, (b) $x = 2.0$, and (c) $x = 7.0$.

Fig. 15 Frequency dependence of a_{33} for the BFS-BT-Mn- x ceramics with (a) $x = 0$, (b) $x = 2.0$, and (c) $x = 7.0$.

Table 1 Refined structural parameters of BFS-BT-Mn-*x* (*x* = 0, 2.0 and 7.0)*ceramics*

Parameters	<i>x</i> = 0	<i>x</i> = 2.0	<i>x</i> = 7.0
Refined factor (%)			
R_{wp}	10.40	11.40	12.80
R_{exp}	9.37	5.82	6.84
$S=R_{wp}/R_{exp}$	1.11	1.96	1.87
Atomic coordinates			
Bi/Ba	0,0,-0.0099(3)	0,0,0	0.004(1),0,0.098(4)
Fe/Ti/Sc/Mn	0,0,0.170(2)	0.530(1),0,0.530(2)	0.480(2),0,0.585(5)
O1	0.463(3),-0.022(3),0.932(3)	0.4235,0,0.0090	0.4235,0,0.0090
O2	–	0.2400,0.24530,0.47800	0.2400,0.24530,0.47800
Lattice parameters			
<i>a</i>	5.6371	5.6507	5.644
<i>b</i>	5.6371	5.6485	5.6444
<i>c</i>	13.8992	3.9910	3.9951
<i>V</i>	382.5032	127.3846	127.2719
Space-group	<i>R3c</i> (Rhombohedral)	<i>C1m1</i> (Monoclinic)	<i>C1m1</i> (Monoclinic)

Table 2 d_{33} , T_C and T_d of the piezoelectric ceramics.

systems	d_{33} (pC/N)	T_C (°C)	T_d (°C)	ref
Pb(Mg _{1/3} Nb _{2/3})O ₃ -Pb(Zn _{1/3} Nb _{2/3})O ₃ -	351	322	320	Chao ⁴⁷
Pb(Zr _{0.52} Ti _{0.48})O ₃ +0.13wt%Ba(W _{1/2} Cu _{1/2})O ₃	470	420	260	Liao ⁴⁸
0.35BiScO ₃ -0.6PbTiO ₃ -0.05(Zn _{1/3} Nb _{2/3})O ₃	28	655	500	Gao ⁴⁹
Ca _{0.9} (Li _{0.5} Ce _{0.25} Pr _{0.25}) _{0.1} Bi ₂ Nb ₂ O ₉	17.3	939	700	Peng ⁵⁰
Ca _{0.95} Sm _{0.05} Bi ₂ Nb ₂ O ₉	11.5	936	900	Chen ⁵¹
0.96K _{0.5} Na _{0.5} Nb _{0.98} Sb _{0.02} O ₃ -0.04Bi _{0.5} Na _{0.5} ZrO ₃	257	300	230	Wang ⁵²
(K _{0.5} Na _{0.5}) _{0.96} Li _{0.04} Nb _{0.775} Ta _{0.275} O ₃	208	320	300	Lin ⁵³
Bi _{0.5} Na _{0.5} TiO ₃	83	360	168	Xu ⁵⁴
0.94Bi _{0.5} Na _{0.5} TiO ₃ -0.06BaTiO ₃	176	288	105	Xu ⁵⁴
0.925Bi _{0.5} Na _{0.5} TiO ₃ -0.075Bi _{0.5} Li _{0.5} TiO ₃	121	402	114	Lin ⁵⁵
0.5Ba(Zr _{0.2} Ti _{0.8})O ₃ -0.5(Ba _{0.7} Ca _{0.3})TiO ₃	441	90	80	Su ⁵⁶
Ba _{0.9} Ca _{0.1} Ti _{0.9} Zr _{0.1} O ₃ +1mol%CuO	360	85	70	Lin ⁵⁷
0.725BiFeO ₃ -0.275BaTiO ₃	136	485	420	Yang ⁵⁸
0.71BiFe _{0.9} (Zn _{1/2} Ti _{1/2}) _{0.1} O ₃ -0.29BaTiO ₃	163	428	380	Shan ⁵⁹
0.72BiFe _{0.99} Al _{0.01} O ₃ -0.28BaTi _{0.97} Zr _{0.03} O ₃	157	435	425	Cen ⁶⁰
0.71BiFeO ₃ -0.29BaTi(Mg _{1/3} Nb _{2/3})O ₃	158	453	400	Zhou ⁶¹
0.725BiFe _{0.96} Sc _{0.04} O ₃ -0.275BaTiO ₃ +0.5mol%MnO ₂	143	596	425	This work

Fig. 1

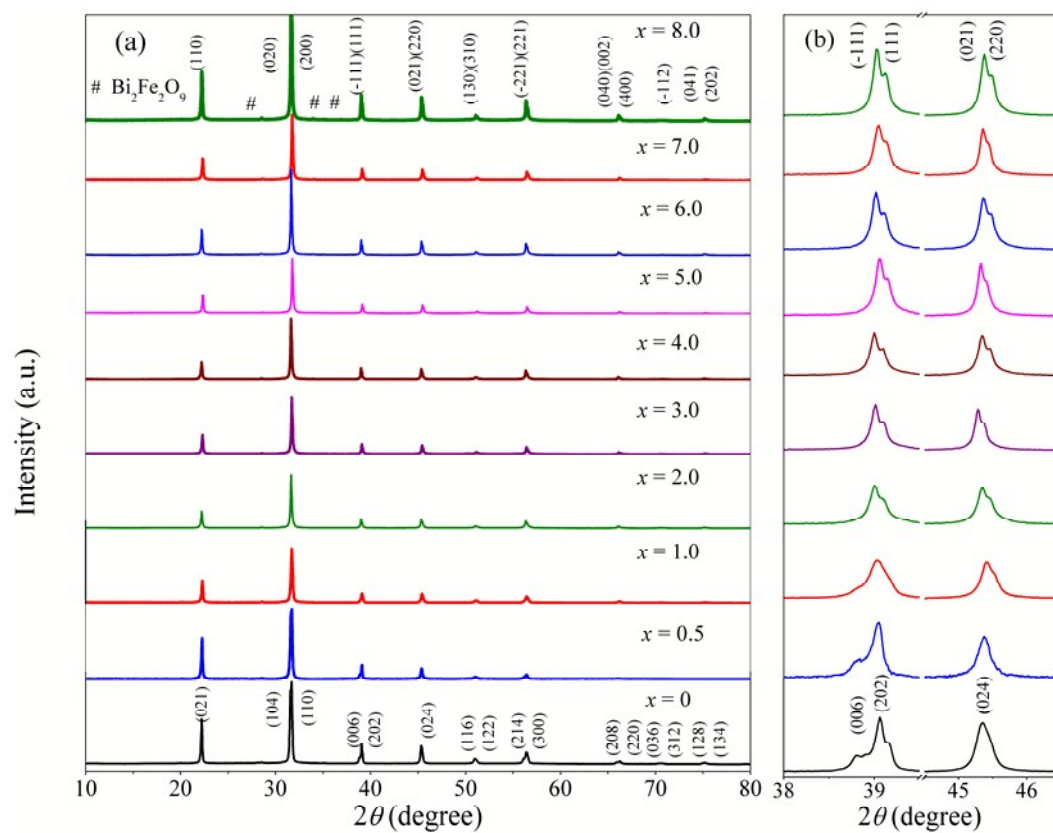


Fig. 2

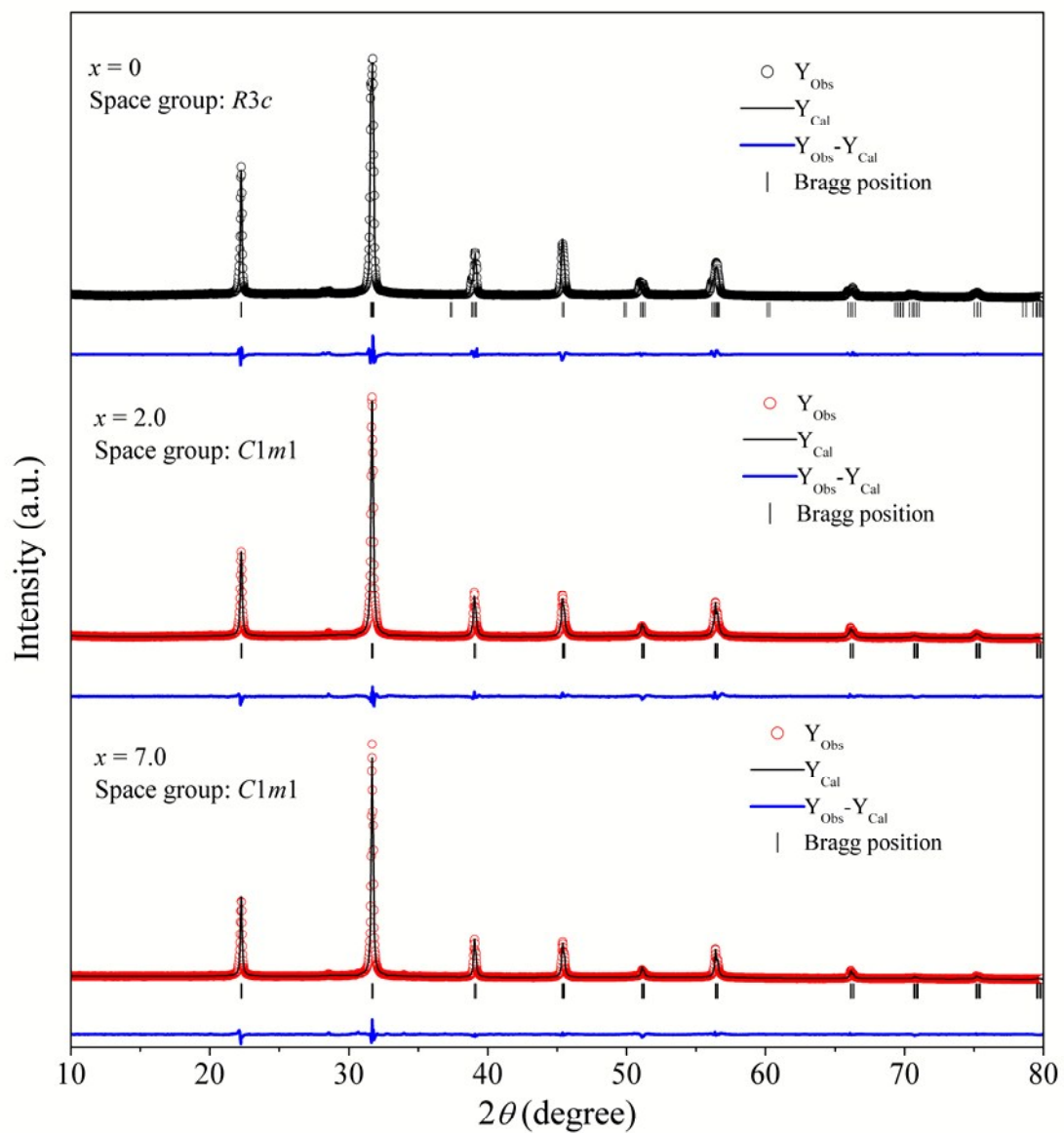


Fig. 3

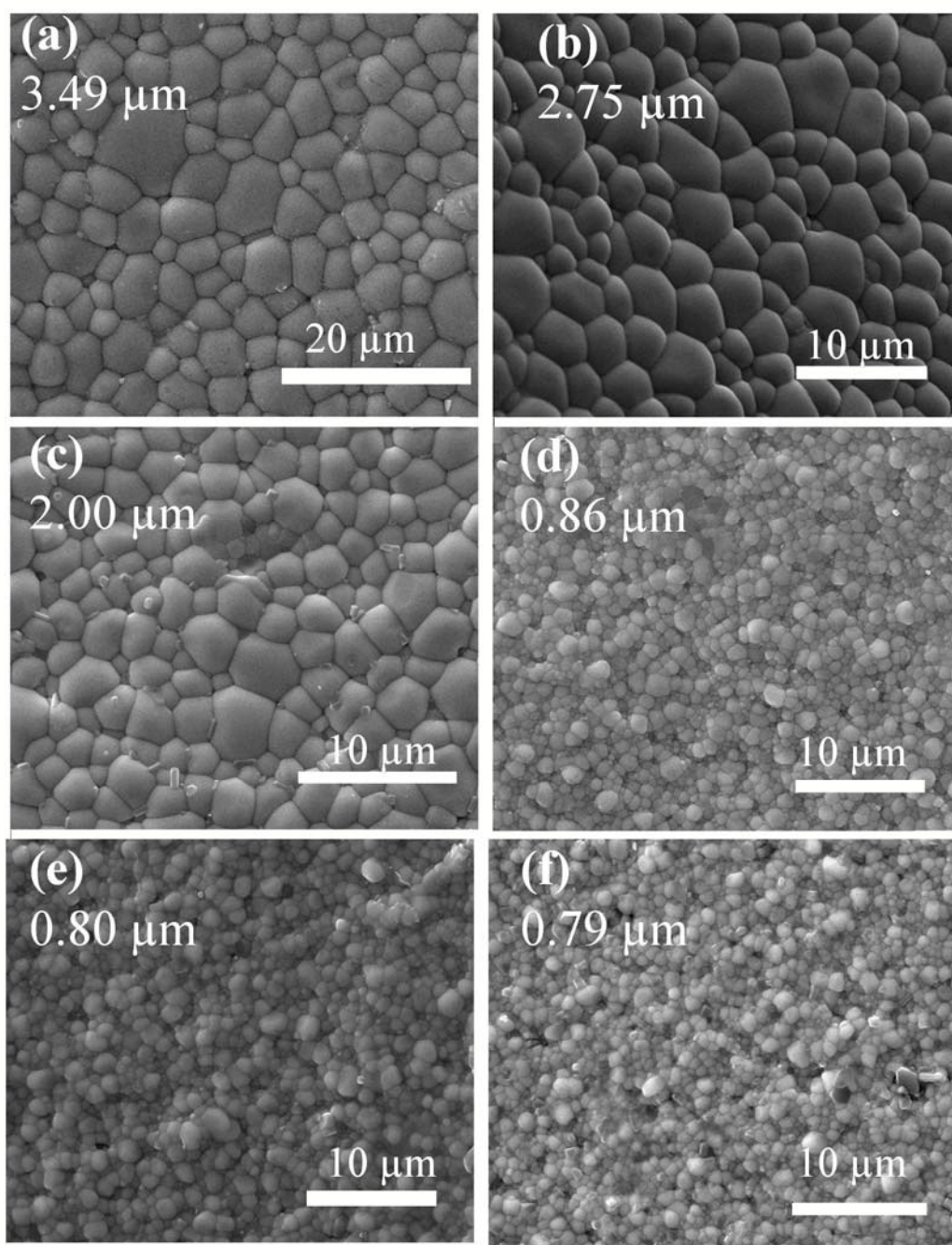


Fig. 4

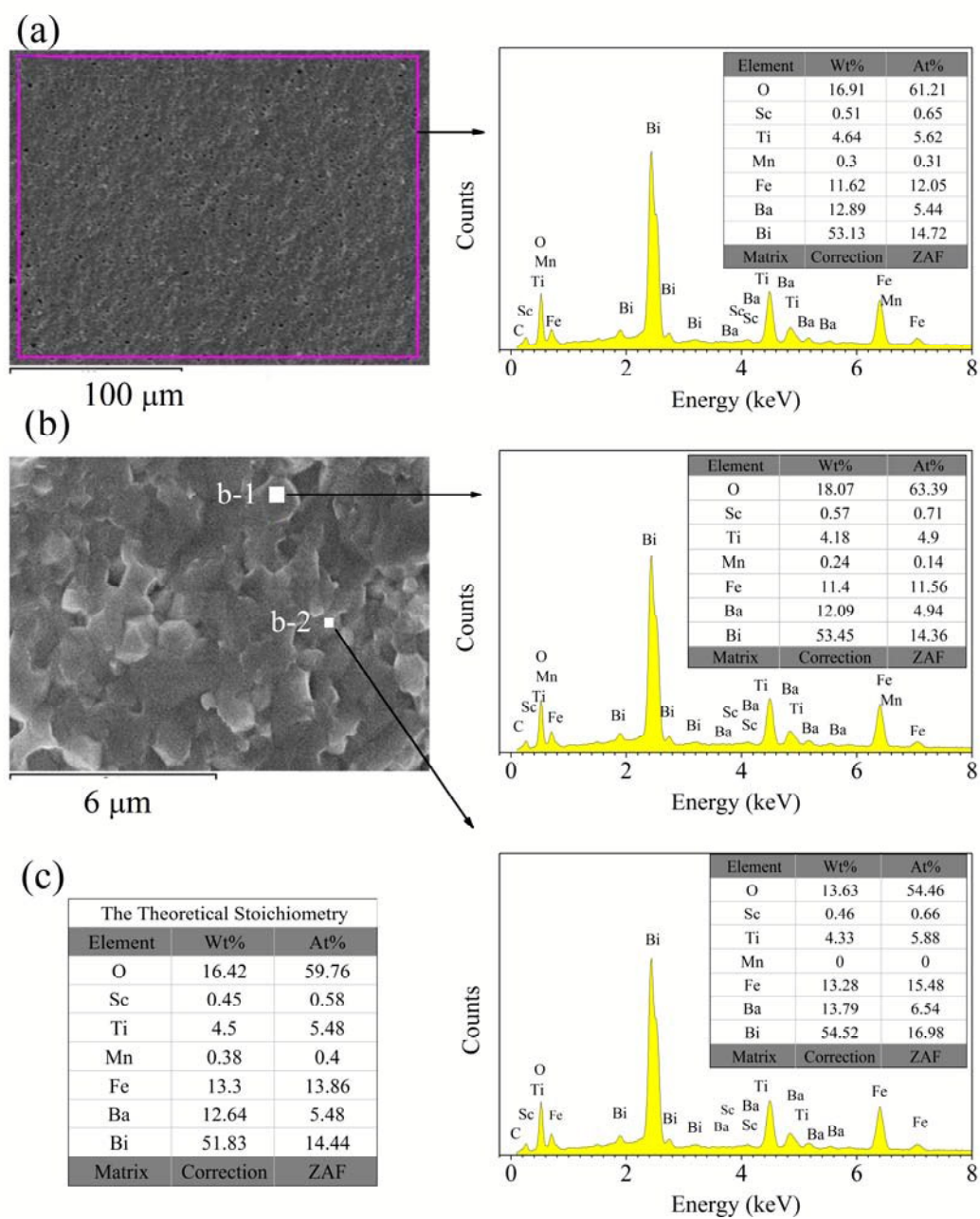


Fig. 5

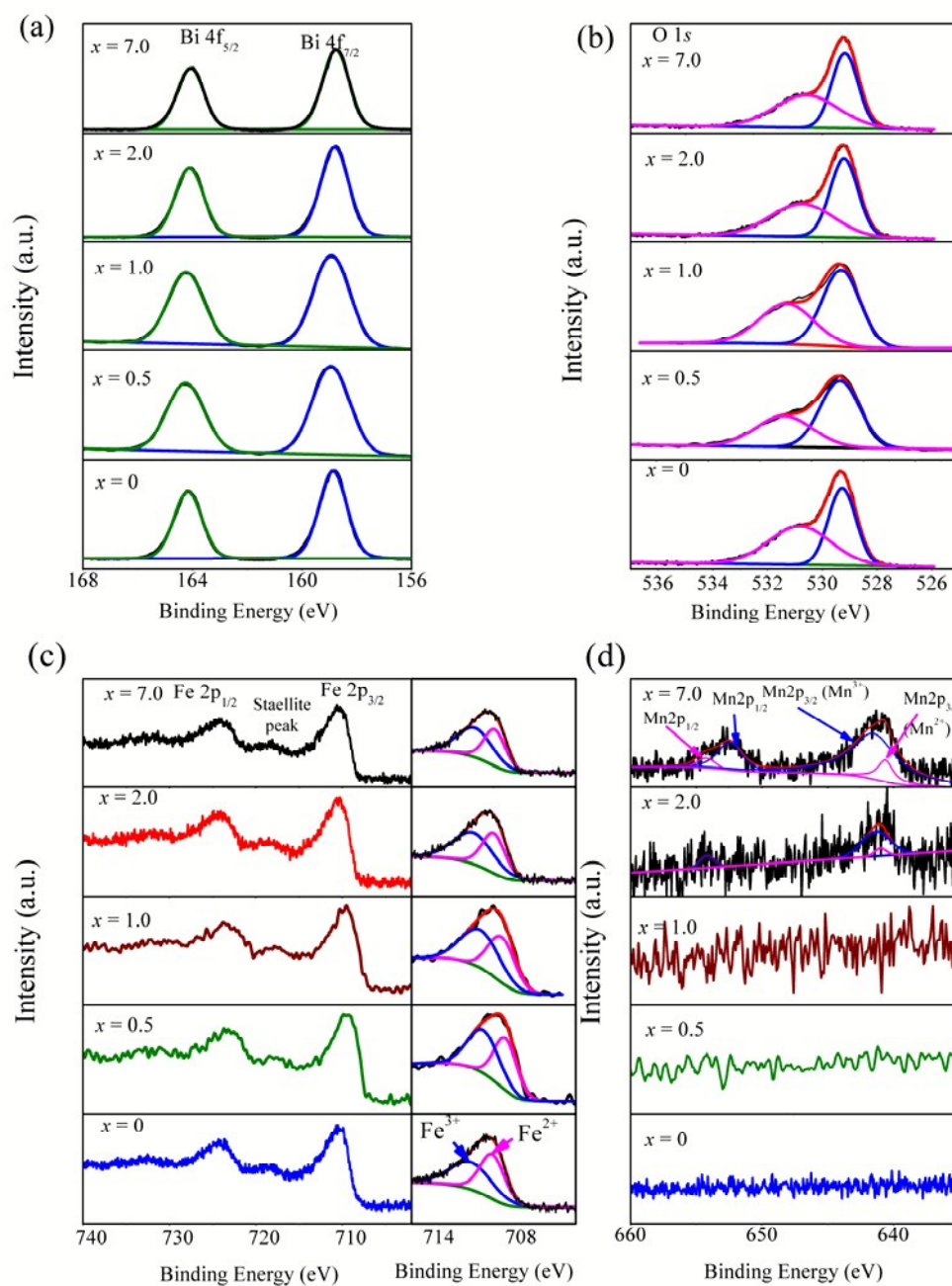


Fig. 6

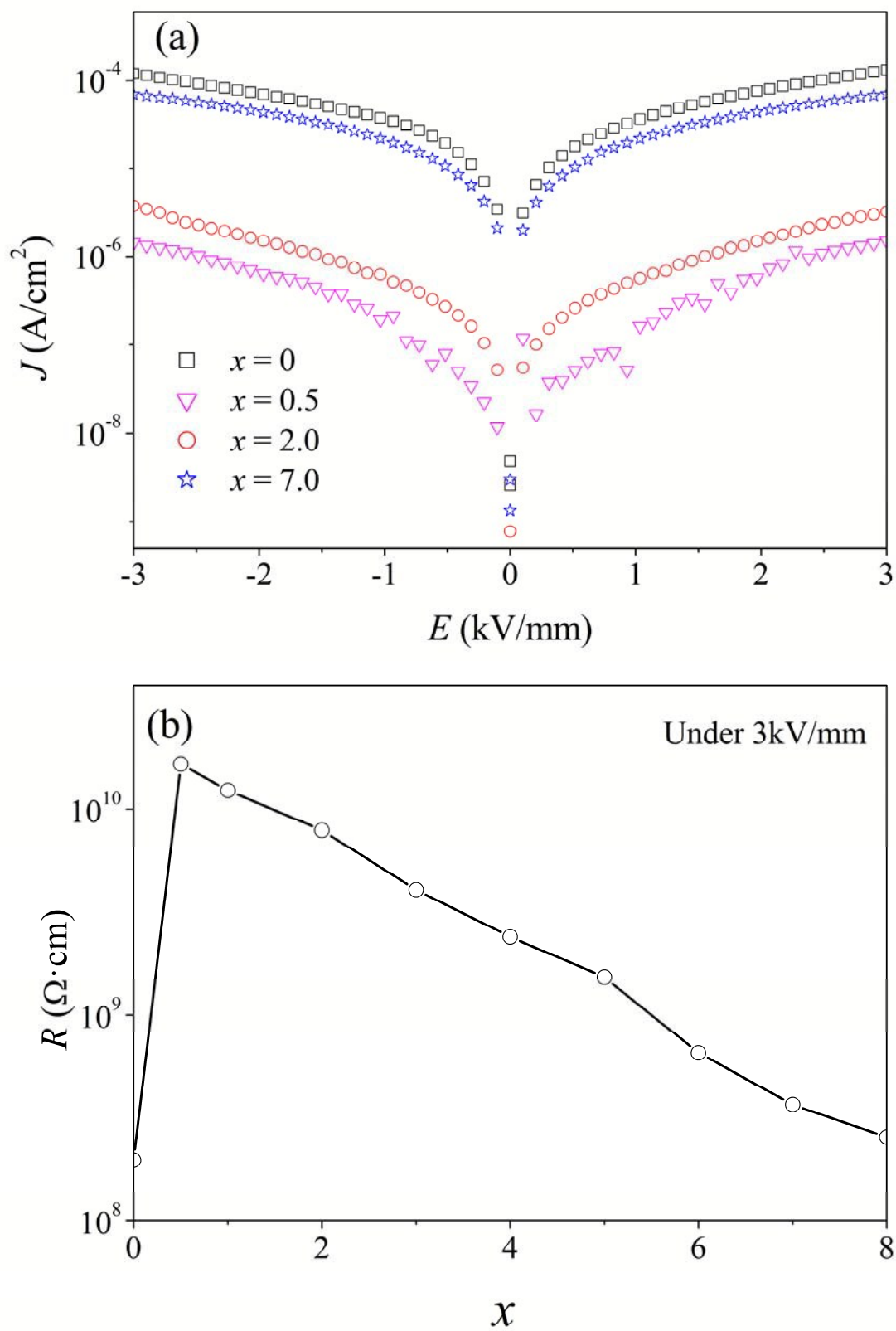


Fig. 7

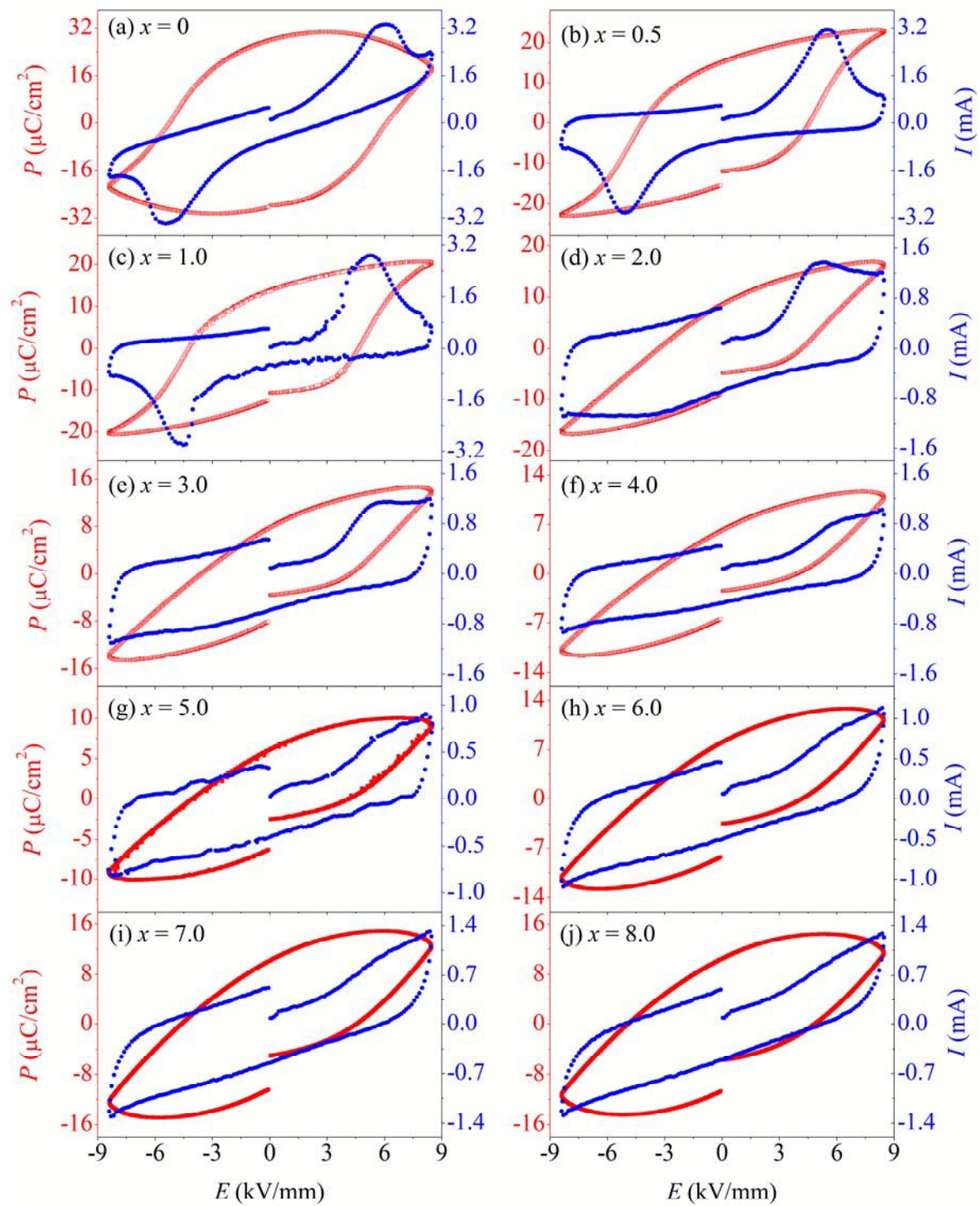


Fig. 8

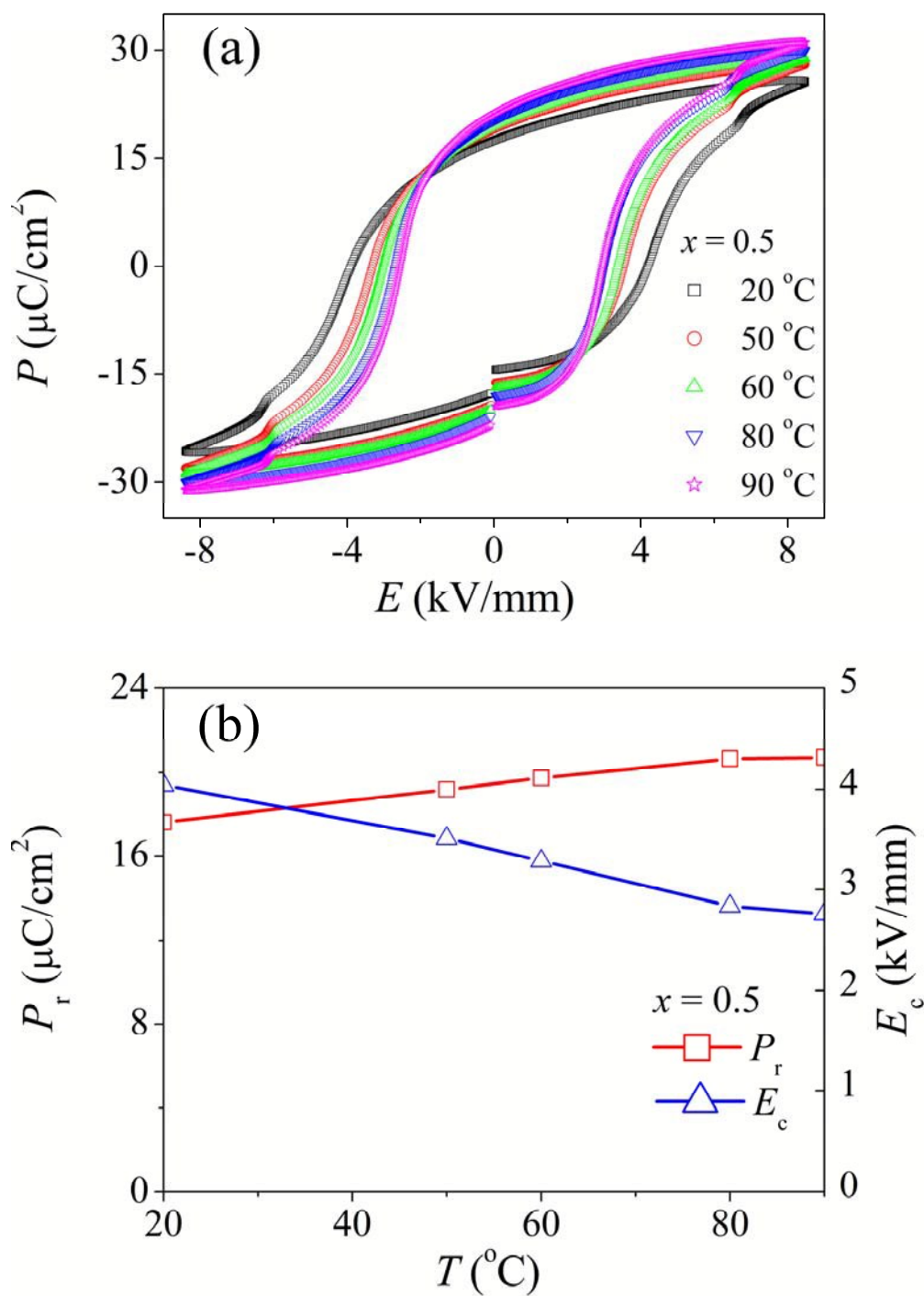


Fig. 9

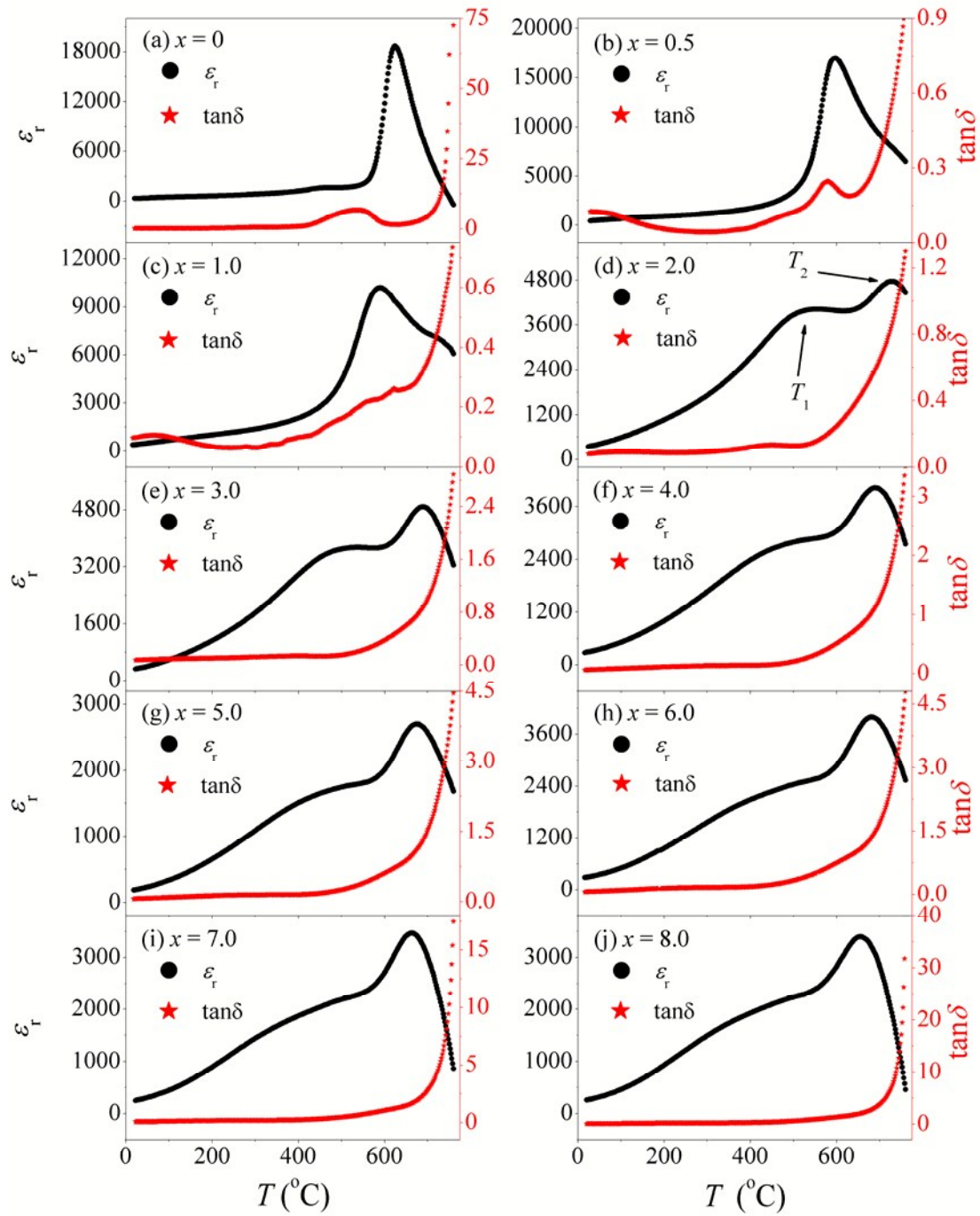


Fig. 10

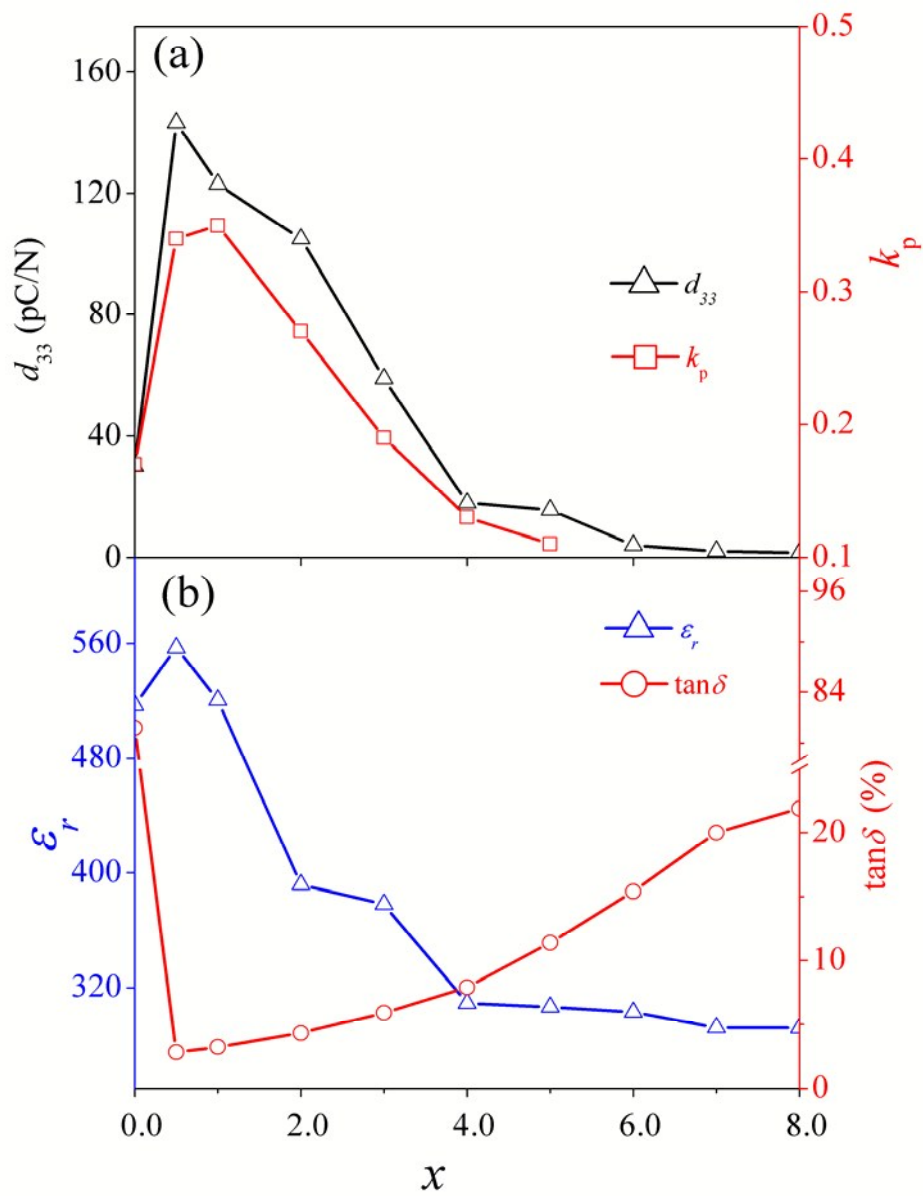


Fig. 11

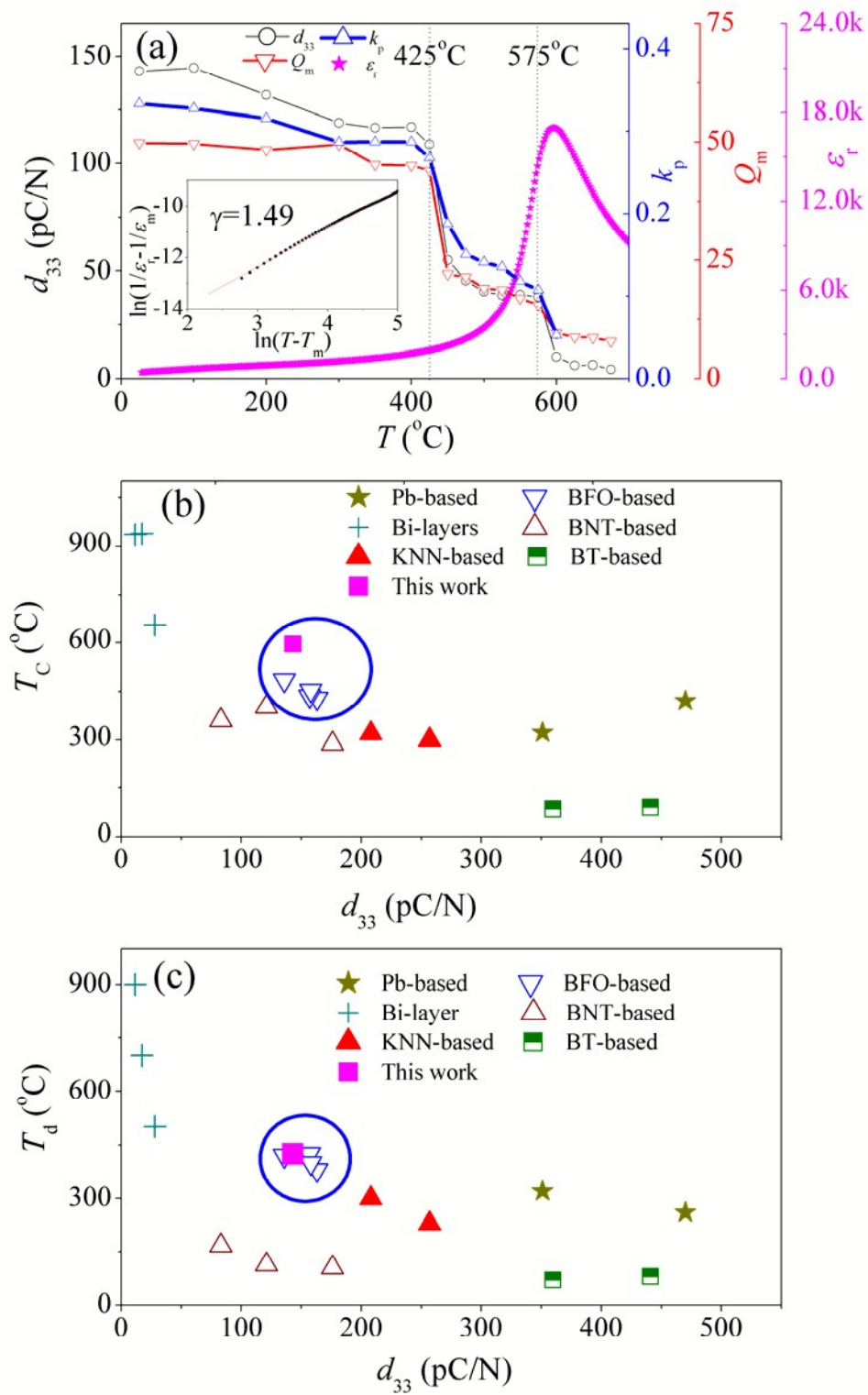


Fig. 12

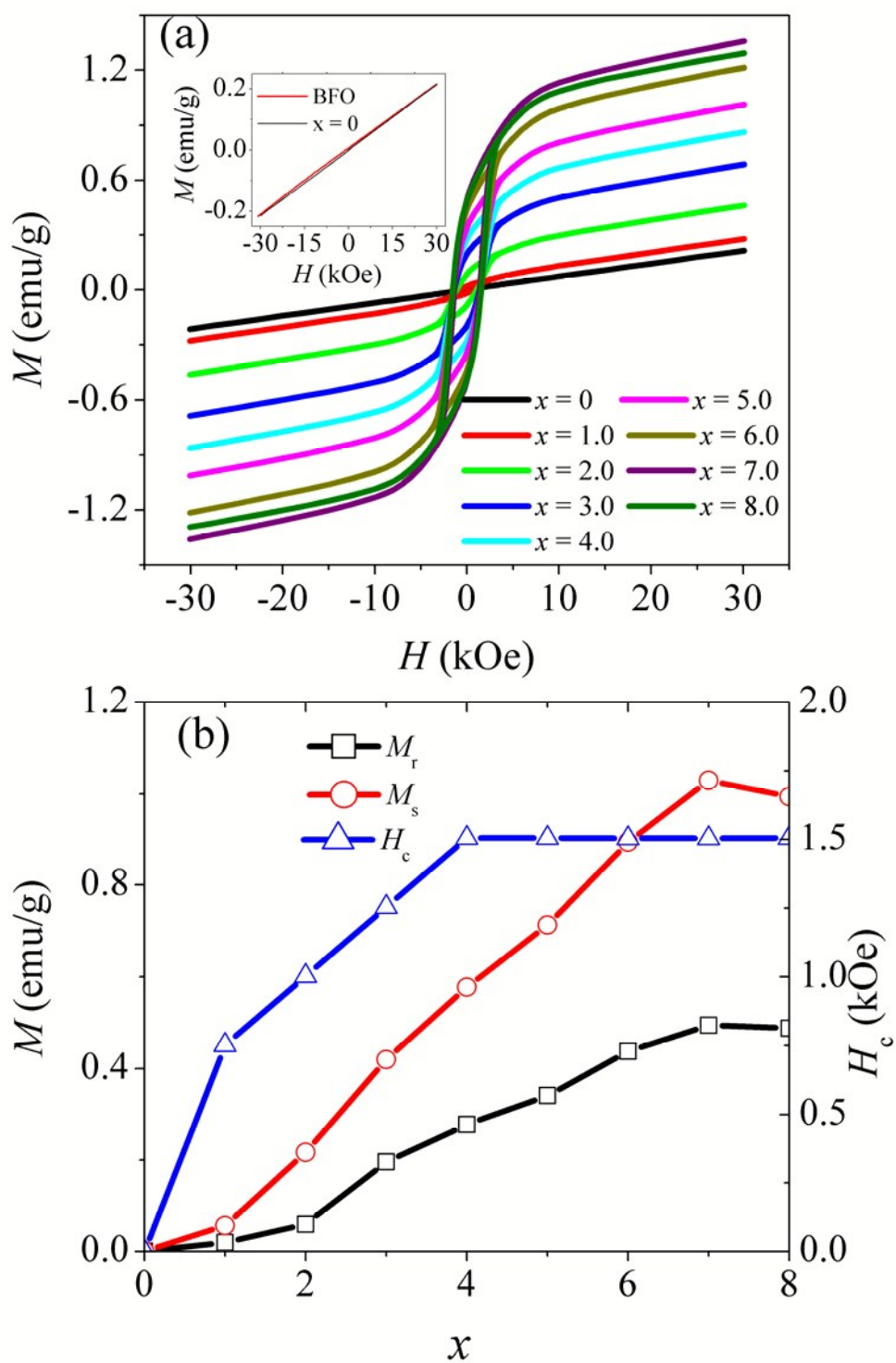


Fig. 13

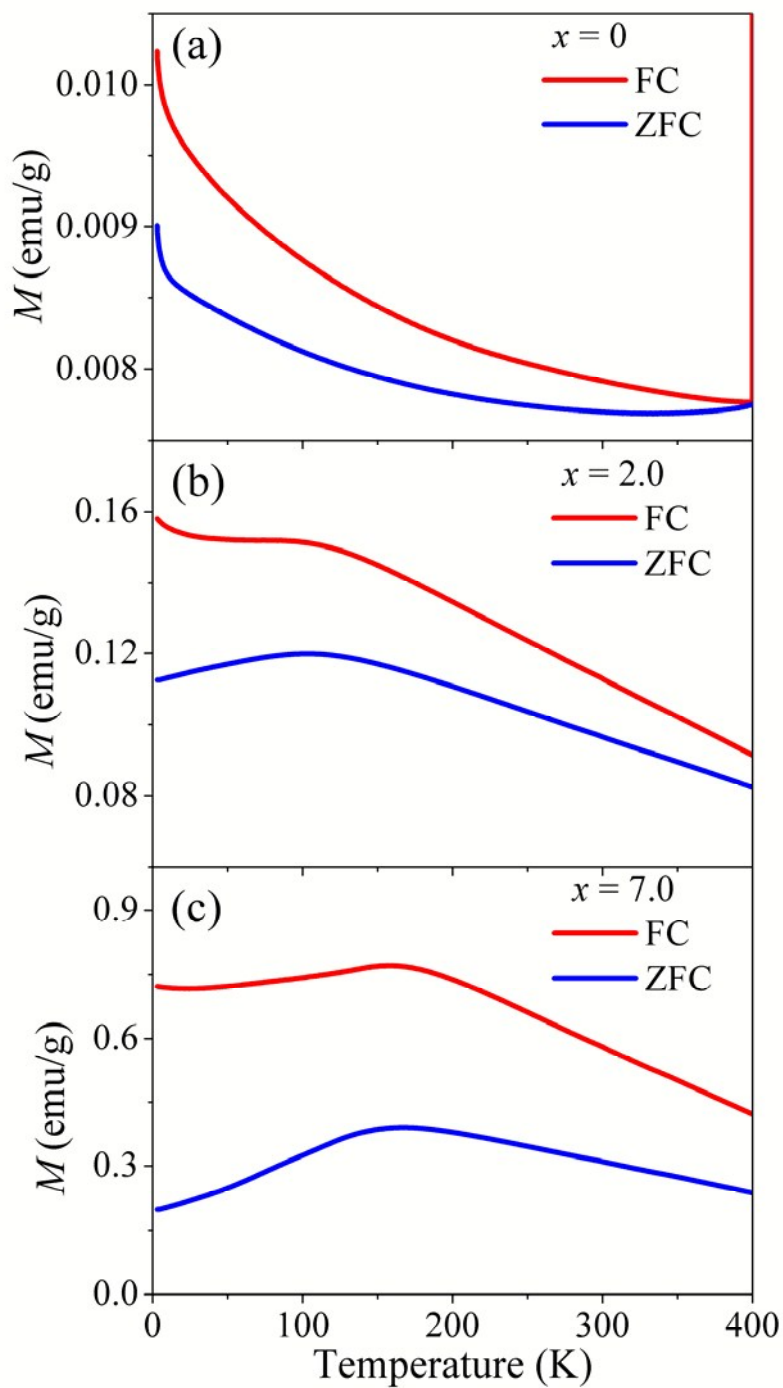


Fig. 14

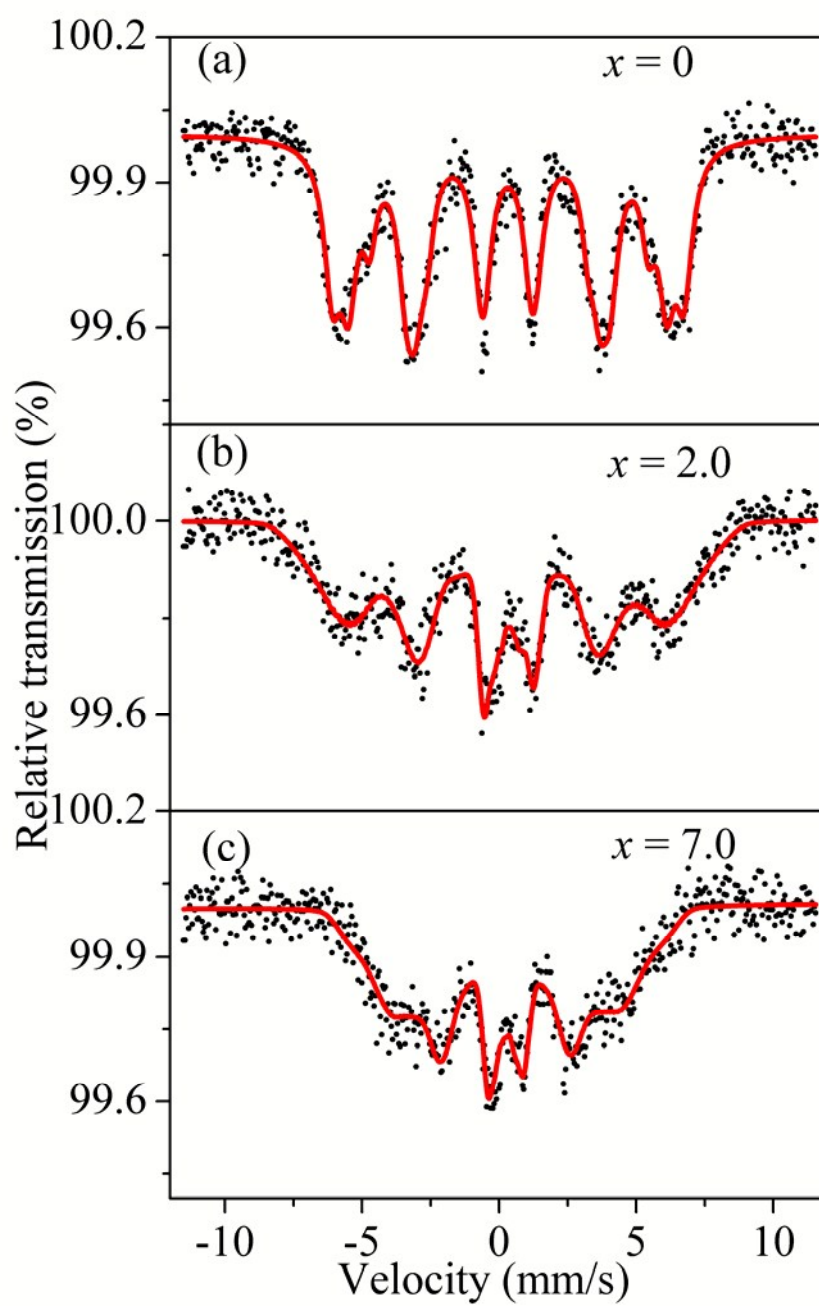


Fig. 15

